Experimental Evaluation and Numerical Modeling of Wide-Flange Steel Columns Subjected to Constant and Variable Axial Load Coupled with Lateral Drift Demands

Julien Cravero, Ahmed Elkady, Dimitrios Lignos

To cite this version:

Julien Cravero, Ahmed Elkady, Dimitrios Lignos. Experimental Evaluation and Numerical Modeling of Wide-Flange Steel Columns Subjected to Constant and Variable Axial Load Coupled with Lateral Drift Demands. Journal of Structural Engineering, 2020, 146 (3), pp.2499. 10.1061/(ASCE)ST.1943-541X.0002499 . hal-04672340

HAL Id: hal-04672340
https://hal.science/hal-04672340v1

Submitted on 18 Aug 2024

Experimental Evaluation and Numerical Modeling of Wide-Flange Steel Columns Subjected to Constant and Variable Axial Load Coupled with Lateral Drift Demands

Julien Cravero[1]; Ahmed Elkady[2]; and Dimitrios G. Lignos[3], M. ASCE

Abstract: This paper presents results from an experimental evaluation on the pre- and post-buckling behavior of 12 steel wide-flange cantilever columns under axial load and lateral drift demands. The influence of several loading and geometric parameters, including the cross-sectional local web and flange slenderness ratios, applied axial load, and lateral and axial loading history on the performance of these columns is thoroughly examined. The test data indicate that cross-sectional local buckling is highly asymmetric in steel columns under variable axial load. A relatively high compressive axial load can significantly compromise the steel column seismic stability and ductility but this also depends on the imposed lateral loading history. The AISC axial load-bending moment interaction equation provides accurate estimates of a steel column's yield resistance. However, the same equation underestimates by at least 30% the column's peak resistance regardless of the loading scenario. Measurements of column flange deformation, axial shortening, flexural resistance and lateral drift are combined in a single graphical format aiding the process of assessing steel column repairability after earthquakes. The test data suggest that current practice-oriented nonlinear component modeling guidelines (PEER/ATC 2010) may not provide sufficient accuracy in establishing both the monotonic and first-cycle envelope curves of steel columns. It is also shown that high-fidelity continuum finite element models shall consider geometric imperfections of proper magnitude in addition to the steel material inelasticity to properly simulate the inelastic buckling of wide-flange steel columns and generalize the findings of physical tests. Issues arising due to similitude are also discussed to properly limit steel column instability modes in future studies.

---

[1] PhD candidate, HMCO|Navier, Ecole des Ponts ParisTech, Champs-sur-Marne, France. E-mail: julien.cravero@enpc.fr

[2] Postdoctoral research scientist, RESSLab, ENAC, Swiss Federal Institute of Technology, Lausanne (EPFL), Lausanne, Switzerland. E-mail: ahmed.elkady@epfl.ch

[3] Associate professor, RESSLab, ENAC, Swiss Federal Institute of Technology, Lausanne (EPFL), Lausanne, Switzerland. E-mail: dimitrios.lignos@epfl.ch

Keywords: Steel columns; Large-scale testing; Axial shortening; Axial load carrying capacity; Column repairability curve; Nonlinear modeling of steel columns; ATC 72; Continuum finite element models; Scale effects

Introduction

Steel columns are essential structural components in preventing earthquake-induced collapse of steel frame buildings. For this purpose, capacity design principles are employed to limit inelastic energy dissipation to selected structural fuses, such as steel beams in steel moment-resisting frames (MRFs) or steel braces in concentrically braced frames (CBFs). However, first-story steel MRF columns near their base are still likely to experience inelastic rotation demands due to the deformation kinematics of a full-frame yield mechanism. Albeit capacity-design protection is applied, steel frame buildings may still experience unanticipated column plastic hinging at higher stories due to force redistributions occurring after the onset of component deterioration in strength and stiffness (Lignos et al. 2011b; Lignos et al. 2013; Tirca et al. 2015; Stoakes and Fahnestock 2016; Nakashima et al. 2018) or due to higher mode effects (Gupta and Krawinkler 2000; Alavi and Krawinkler 2004; Tremblay 2018).

Although columns in prospective steel MRF designs typically experience modest axial load demands of up to 30% of their axial yield strength, P_y, (NIST 2010a; Elkady and Lignos 2014; Suzuki and Lignos 2014; Elkady and Lignos 2015b), in existing steel MRF tall buildings, their columns may experience axial load demands on the order of 50%~70% P_y (Bech et al. 2015; Akcelyan and Lignos 2018). From a retrofit perspective, it may be challenging to retain a cost efficiency because the ASCE 41 standard (ASCE 2014) would treat these columns as forced-controlled elements (i.e., zero plastic deformation capacity), regardless of their respective local cross-sectional and member slenderness geometric properties. This assumption was mostly justified based on research conducted in the early 1970s on small-scale column specimens (Popov et al. 1975). However, recent work (Newell and Uang 2006; Elkady and Lignos 2016; Ozkula et al. 2017; Elkady and Lignos 2018a, b) suggests that the same assumption may not be justifiable for "stocky" wide-flange columns with web slenderness ratios $h/t_w < 20$ and member slenderness ratios $L_b/r_y \leq 80$ (L_b is the column's unbraced length; r_y is the cross-section's radius of gyration with respect to its weak-axis). However, available experimental data on steel columns subjected to high compressive axial load demands ($\geq 0.5P_y$) coupled with lateral drift demands is still scarce to further substantiate a potential change of the corresponding limit for force-controlled elements as well as the current ANSI/AISC 360-16 (AISC 2016) axial compressive limit of $0.75P_y$ for the plastic design of steel columns with plastic hinges. This data could also be potentially useful for the seismic design of steel CBF columns. Although these are primarily subjected to high axial load demands, the column flexural demands could considerably increase due to the non-uniform inelastic drift demands along the steel CBF height (Toutant et al. 2017).

From a repairability stand point, FEMA P58 (FEMA 2009a) provides recommendations for typical repair measures and their cost estimates for damage states associated with flexural yielding, cross-sectional local buckling and weld fracture in the aftermath of earthquakes. However, these are mostly applicable to steel beams in fully restrained beam-to-column connections. Although some of these measures (e.g. heat straightening) may be applicable to steel columns, these repairs could become challenging due to potential residual axial shortening (MacRae et al. 1990; Ozkula et al. 2017; Elkady et al. 2018; Elkady and Lignos 2018a). Depending on the cross-sectional slenderness, the reserve capacity of a steel column after a seismic event may not necessarily be much depending on the imposed lateral drift demands.

From a nonlinear modeling stand point, current guidelines for performance-based seismic design and assessment (LATBSDC 2017; PEER 2017) of new and existing steel buildings necessitates the use of component hysteresis models of varying complexities to properly trace the onset of geometric instabilities (e.g. local buckling and lateral torsional buckling) that could significantly compromise the structural behavior at ultimate limit states. This is also an apparent necessity to properly characterize the collapse risk of prospective designs that consider new lateral load resisting systems based on formally established collapse risk-assessment methodologies (FEMA 2009b). Current guidelines (PEER/ATC 2010) facilitating the above needs, mainly cover modeling recommendations for concentrated plasticity phenomenological deterioration models (e.g., Ibarra et al. 2005) due to their computational efficiency. These recommendations were primarily benchmarked to experimental data from fully restrained beam-to-column connections that became available after the 1994 Northridge earthquake (FEMA 2000; Lignos and Krawinkler 2011, 2013). Therefore, their applicability to the nonlinear modeling of steel columns shall be carefully examined since PEER/ATC (2010) modeling guidelines neglect important loading (e.g., axial load) and geometric parameters (e.g., L_b/r_y) that may significantly affect the column behavior under cyclic loading. The need for more monotonic test data in addition to the ones based on reversed cyclic loading is also apparent (Haselton et al. 2008; Krawinkler 2009; Maison and Speicher 2016). The reason is that a monotonic backbone curve, which is considered as a unique property of a structural component, is typically used to benchmark models that explicitly capture component cyclic deterioration in strength and stiffness for use in nonlinear dynamic analysis (Lignos and Krawinkler 2011; Hamburger et al. 2018).

Furthermore, with computational advancements and the use of high-performance computing, high fidelity continuum finite element (CFE) models are used more and more in explicit collapse simulations of steel frame buildings (Miyamura et al. 2015; Wu et al. 2018a). Despite of the associated computational cost, challenges in this case arise on how to reliably trace the onset and progression of geometric instabilities, as well as the potential coupling of different instability modes, in an explicit manner such that cyclic deterioration in flexural and axial strength of the column can be reliably predicted. Several modeling proposals are available regarding the above matters (Newell and Uang 2006; Elkady and Lignos 2015a; Araújo et al. 2017; Elkady and Lignos 2018b; Wu et al. 2018b) with conflicting recommendations. In that respect, column physical experiments can benchmark various modeling options and provide coherent recommendations for high fidelity CFE modeling. These models could significantly expand the range of available steel column data by considering a broader range of parameters and configurations that may not be feasible to be physically tested. As such, experiments and complementary CFE simulations can address future challenges regarding the seismic design of steel structures (Uang and Bruneau 2018).

With the goal of further comprehending the hysteretic behavior of wide-flange steel columns to address most of the above challenging issues, this paper summarizes the findings from an experimental program involving 12 large-scale wide flange steel columns tested in a cantilever fashion. The specimens are approximately two-thirds of full-scale as compared to columns used in typical steel frame buildings designed in seismic regions. The loading schemes comprise monotonic and reversed cyclic lateral drifts coupled with relatively high constant and variable axial load demands. The tests reported herein are part of a broader research study that examines the seismic stability of steel columns due to local and member instabilities, considering the development and validation of component modeling techniques of various fidelities for the seismic assessment of steel members and structures.

Description of the Test Program

Table 1 summarizes the test matrix parameters. Three cross-sections are utilized: W14x61 (Group A), W16x89 (Group B) and W14x82 (Group C). Each group includes four nominally identical specimens. These sizes are representative of first-story columns in mid-rise MRFs (4 to

8 stories) at a two-third scale. The W14x82 and W16x89 cross-sections satisfy the ANSI/AISC 341-16 (AISC 2016a) compactness limits for highly ductile members, λ_{hd}, regardless of the applied compressive axial load ratio, P/P_y (P is the applied axial load; P_y is based on the measured geometric and material properties of a specimen). These two cross-sections have similar flange slenderness ratios ($b_f/2t_f = 5.9$) but different web slenderness ratios. The W14x61 cross-section has a flange slenderness ratio ($b_f/2t_f = 7.8$) slightly higher than the ANSI/AISC 341-16 flange compactness limit for highly ductile members (λ_{hd}=7.2).

The test specimens, which were manufactured from three different steel heats, are fabricated from ASTM (2015) A992 Grade 50 steel (nominal yield stress, f_{yn} = 345MPa). The material properties and chemical composition based on the mill certificate are summarized in Table 1 and Table 2, respectively. The same table reports the measured steel material properties based on uniaxial tensile coupon testing (ASTM 2014). The reported values are the average ones from three coupons extracted from a cross-section's web and flanges. In brief, the steel materials in Groups A, B, and C have a measured yield stress, f_y, that is 6%, 9%, and 16% larger than the nominal one, respectively. These values are consistent with the expected-to-nominal yield stress ratio, R_y, of 1.1 for ASTM A992 Grade 50 steel (AISC 2016a).

Figure 1 shows the overall test setup used for the experimental testing of cantilever steel column specimens. The setup comprises a 12MN high capacity vertical actuator and a 1MN horizontal actuator with a ±250mm stroke. In-plane bracing is employed as shown in Fig. 1 to provide in-plane lateral stability to the 12MN vertical actuator. Both actuators are connected, through axially rigid links, to a high precision structural pin at the column specimen's top end. This pin represents a column's inflection point at mid-height by assuming idealized fixed-end boundary conditions at both column ends. Two running beams (noted as guide beams) provide lateral stability bracing at the column specimen's top end. Referring to Fig. 2, the column specimens have a clear length, L, of 1750mm and a base-to-pin length of 2150mm. End plates are welded at both column ends with complete joint penetration (CJP) J-groove welds as shown in Fig. 2. The welds were inspected with ultrasonic testing to ensure that potential defects were below the allowable limits as per AWS (2009). The weld access holes are designed as per Section J1.6 of AISC (2016b) to ensure minimum stress concentrations at the current weld location.

The test program incorporates three lateral loading protocols. These include: i) a monotonic protocol to obtain the monotonic backbone curve of each column specimen at representative gravity-induced axial load ratios and ii) the standard AISC (2016a) symmetric cyclic protocol (Clark et al. 1997), which is commonly used in the pre-qualification of fully restrained beam-to-column connections. In an effort to reduce the total testing time, the symmetric protocol was slightly modified by reducing the number of elastic cycles at the 0.375%, 0.5% and 0.75% drift amplitudes (see Fig. 3a). Lastly, a collapse-consistent lateral loading protocol (Suzuki and Lignos 2014) is also employed to investigate the influence of the lateral loading history (i.e., cumulative damage) on a steel column's hysteretic behavior (see Fig. 3b). This protocol represents the seismic demands in steel MRF columns at large deformations associated with structural collapse (Ibarra and Krawinkler 2005; Lignos et al. 2011a). If after the first loading phase, the steel column flexural resistance is still higher than 50% of its peak flexural resistance, then this protocol is repeated as shown in Fig. 3b. The lateral drift protocols are coupled with constant compressive axial load ratios of 0.3 and 0.5 (see Table 1). A higher axial load ratio of 0.75 was also used to re-assess the ASCE/SEI 41-13 (ASCE 2014) axial load limit for force-controlled elements. Although this axial load demand largely exceeds that expected in steel MRFs (Elkady and Lignos 2014; Suzuki and Lignos 2014), it could be representative in steel CBF columns (Toutant et al. 2017). The symmetric cyclic lateral loading protocol is synchronized with variable axial load demands representing the loading conditions of steel MRF end columns due to dynamic overturning effects (i.e., transient axial load component). The first axial load protocol has a gravity offset, P_g, of 0.30 P_y and a transient component, P_v, of ±0.45 P_y (i.e., reaching 0.15 P_y in tension and 0.75 P_y in compression as shown in Fig. 3c). The second one involves a gravity load offset of 0.50 P_y and a transient component of ±0.25 P_y (see Fig. 3d). The imposed axial loading protocols are fairly conservative because after the onset of column geometric instabilities, the axial load demands are typically relaxed due to force redistributions (Suzuki and Lignos 2014).

Instrumentation and Deduced Column Response Parameters

A total of 27 uniaxial strain gauges are installed on each specimen's web and flanges near their column base over a length of 1.6 d (d is the column depth) to track the onset of flexural yielding and plastic strain progression. String potentiometers are used to monitor the in-plane lateral displacement as well as the axial shortening, Δ_{axial}, of a column's top end. Linear variable differential transformers (LVDTs) and inclinometers, installed on a specimen's bottom base plate confirmed the assumption of the fixed end boundary since there was no indication of base plate slip and uplift during the tests. Light-emitting diode (LED) targets are used to track the out-of-plane displacements (δ_{op}) along the column height as shown in Fig. 4. These are also used to track the in-plane displacement of the flange tips (δ_f), which is later on used to assess the feasibility of column repair following earthquakes.

Fig. 5 shows the deduced end moment versus the column's chord rotation for all the specimens. Similarly, Fig. 6 shows their axial shortening history versus the column chord rotation. Referring to Fig. 5, the end moment, M, is computed as the summation of the actuators' force components, in the global coordinate system, multiplied by the corresponding lever arms to the top surface of the column base and considering the rigid body rotation of the top pin assembly. The moment is then normalized with respect to the plastic bending resistance, M_p of the corresponding cross-section. The M_p is based on the measured geometric and material properties of the respective test specimen. Figure 7 shows the out-of-plane column displacement, δ_{OP}, and the in-plane flange tip displacement, δ_f, histories versus the chord rotation for selected column specimens as defined in Fig. 4. In Figs 5, 6 and 7 and the subsequent discussion, the chord rotation, θ, is defined as the in-plane lateral displacement at the column top over its clear length, L. In the subsequent sections, a qualitative and quantitative assessment of the steel damage progression is presented including critical aspects associated with the steel column stability under monotonic and cyclic loading.

Qualitative Summary of Column Behavior

The typical damage sequence of a wide-flange steel column often leading up to the complete loss of its axial-load carrying capacity is illustrated in Fig. 8. During small elastic cycles there is no evident deformation in a test specimen. Referring to Fig. 8a, flexural yielding in the column web and flanges typically occurs at chord rotations ranging from 0.25% to 0.65% radians, depending on the cross-section and the imposed axial load demand. This is visually observed through pealing of the mill-scale at the column surface. Shear yielding is also evident in the web (see Fig. 8a). Upon further lateral loading, the column's fixed end experiences local buckling. The peak of the corresponding local buckling wave is observed at a distance of 0.4 to 0.8 d measured from the column base, as seen in Fig. 8b. The local buckling mode(s) and corresponding amplitudes are mainly dependent on the imposed lateral drift history. In particular, specimens subjected to monotonic and collapse-consistent lateral loading histories experience asymmetric local buckling (Fig. 8b). Drifting in one loading direction (Ibarra and Krawinkler 2005) dominates the column response, thereby leading to asymmetric local buckling. On the other hand, columns subjected to a symmetric cyclic lateral loading history coupled with a constant compressive axial load experience symmetric local buckling as indicated in Fig. 8c. This damage pattern is consistent even in cases that although the axial load varies it always remains compressive. Asymmetric local buckling occurs if the axial load demand fluctuates from compression to tension. The reason why the local buckling shape becomes asymmetric in this case is due to neutral-axis shifting that tends to straighten the buckling wave in one of the two loading directions (see Fig. 8e). At larger drift excursions (≥ 3%) a second buckling wave often develops at a distance of 0.8 to 1.6 *d*; hence, a full sinusoidal buckling wave is noticeable (see Figs. 8d and 8e). This second buckling wave is accompanied with large out-of-plane displacements near the column's dissipative zone as shown in Fig. 8f. At a lateral drift of 3%, the out-of-plane displacements of the column plastic hinge reaches about 20mm (1.0% *L*). at this point, the in-plane flange tip displacement is on the order of 40mm (see Fig. 7). The magnitude of these displacements affects the repair actions in steel columns in the aftermath of earthquakes as well as the column's reserve capacity that could be of interest in mainshock-aftershock earthquake series. The above issues are carefully examined in a subsequent section. Referring to Fig. 8f, the observed out-of-plane instability mode is typically followed by a rapid loss of the column's axial load carrying capacity. This is typically accelerated under a high compressive axial load and/or a high web slenderness ratio. Notably, specimens A4, B3 and C4 experienced a sudden loss of their axial load carrying capacity. In particular, in specimen C4 (subjected to 0.75 P_y), axial shortening grew rapidly from 110mm to 170mm (6% to 9% *L*) within few seconds (see Fig. 6i). This indicates the member inability to carry the imposed axial load demand due to the associated instability mode. Referring to Fig. 5i, this corresponds to a complete loss of the column's flexural resistance.

Quantitative Assessment of Column Behavior

The previous section summarized a number of qualitative features characterizing the behavior of steel columns under lateral drift and axial load demands. This section provides a quantitative assessment of the column hysteretic behavior by considering a number of performance indicators including the cyclic deterioration in a column's flexural resistance, the column axial shortening and the associated plastic hinge length. The influence of the axial load variation on a column's hysteretic response is carefully examined. Issues related to similitude for experimental testing of steel columns are also investigated by means of comparisons with experimental data from prior column testing programs. Finally, based on a synthesis of experimental results, the concept of a column's repairability curve is introduced that may facilitate decision-making for steel column repairs in the aftermath of earthquakes.

Column Flexural Resistance

Figure 5 shows the moment-rotation relation of the tested specimens. Steel columns experience flexural strength deterioration due to local buckling-induced softening regardless of the employed loading conditions and cross-sectional geometric properties. This is attributed to the relatively small member slenderness ratios ($L_b/r_y < 30$) in all cases. Only in few cases, plastic lateral torsional buckling is coupled with local buckling but only at large drift demands. For instance, for specimen B2 (W16x89, P/P_y=0.5), this only occurred after 8% radians under monotonic loading resulting into a steeper negative stiffness in the post-peak response (see Fig. 5d).

Under monotonic lateral loading (see Figs. 5a, 5d, 5g), the tendency for local buckling initiation decreases with decreasing local web and/or flange slenderness ratios, resulting in increased pre-peak plastic rotation capacities, θ_p (difference between chord rotation at the peak response minus the corresponding column yield rotation). This effect is somewhat pronounced with decreased compressive axial load ratio because a larger portion of the web cross-section experiences tensile stresses at a given lateral drift demand, thereby providing restraint against web local buckling. Figures 5a and 5b suggest that when local buckling is the primary instability mode of wide-flange steel columns (e.g., Specimens A1, A2 and B1), they attain a residual plateau due to local buckling length stabilization (Krawinkler et al. 1983). On the other hand, column specimens experiencing coupled local and lateral torsional buckling under monotonic loading (e.g., Specimen B2) attain a second steeper negative stiffness soon after the onset and progression of local buckling. Although inconclusive, this implies that wide flange beam-columns experiencing coupled geometric instabilities under monotonic loading do not necessarily reach to a residual flexural resistance because a buckling length stabilization path cannot be attained. Figures 5g and 5d indicate that although the local and member slenderness ratios of W16x89 and W14x82 columns are nearly the same (see Table 1), the former has a θ_p of about 4% while the latter has a θ_p of more than 7% at a given compressive axial load demand. This implies that the respective steel material has a strong influence on the steel column plastic deformation. Albeit all columns are fabricated from nominally identical A992 Gr. 50 steel, the chemical composition of Group C include a notably larger percentage of Manganese than that of Groups A and B (see Table 2). This strongly influences the steel material hardenability (Shirasawa et al. 1981; Bruneau et al. 2011) and in turn the plastic deformation capacity of a steel member prior to the formation of local buckling. In particular, specimens C1 and C2 hardened monotonically much more than specimens A1, A2, B1 and B2 as shown in Figs 5g, 5a and 5d, respectively.

Referring to Fig. 5, the hysteretic behavior of wide-flange steel columns under cyclic lateral loading is primarily governed by local buckling in their post-peak response. Columns that are subjected to a constant compressive axial load ratio ($P/P_y \geq 0.5$), experience accelerated cyclic deterioration in their flexural resistance after the onset of local buckling. Although most columns maintained their flexural resistance at a lateral drift of 2%, the ones subjected to a symmetric cyclic lateral loading history lost their axial load carrying capacity at a lateral drift of 4% regardless of their local slenderness ratios. This is mostly attributed to the relatively large number of inelastic drift cycles of a symmetric cyclic lateral loading history. Notably, a W14x61 column (Specimen A3), which is moderately compact as per ANSI/AISC 341-16, maintained close to 80% of its flexural resistance up to a lateral drift demand of 6% when subjected to a collapse-consistent lateral loading protocol (see Fig. 5b). This indicates the strong influence of the imposed lateral loading history on the steel column hysteretic response.

Column specimens subjected to variable axial load demands developed a fully asymmetric hysteretic behavior (see Figs. 5c and 5f). In particular, while the compressive axial load increases in an absolute sense due to the transient axial load demand in addition to the gravity-induced one, the flexural negative stiffness in a column's post-peak response becomes relatively steep. On the other hand, while a column experiences reduced compressive axial load demand in the opposite lateral loading direction, its flexural resistance does not practically deteriorate. This is attributed to local buckling straightening. Notably, the measured data corresponding to Figs. 5c and 5f should be interpreted as lower bounds of a column's behavior under variable axial load demands. The reason is that the imposed axial load demands are relaxed due to force redistributions occurring within a steel frame building experiencing structural damage. This relaxation may reach up to 50% of the initial axial load demand (Suzuki and Lignos 2014, 2015b).

Assessment of Axial Force – Bending Interaction Curves

The experimental data set covers a wide range of axial load demands, offering the opportunity to evaluate the existing axial force-bending (P-M) interaction curves of current code provisions. Figure 9 shows the ANSI/AISC 360-16 (AISC 2016) P-M interaction curve. The vertical and horizontal axes are normalized with respect to the available axial and flexural strengths, P_c and M_c, respectively, according to AISC (2016b). In this computation, the resistance ϕ factors and the measured material properties are considered. The following parameters were also assumed: an effective length in the weak-axis direction L_c=875mm, an unbraced length L_b=L=1750mm and a lateral-torsional buckling modification factor C_b=1.67. In all cases, M_c was controlled by the yield limit state (i.e., $M_c = \phi\ M_p$). Shown in the same figure are all the measured P-M data points when first yield occurred at the extreme fiber (Fig. 9a) and at the maximum attained moment (Fig. 9b). Referring to Fig. 9a, the P-M interaction curve adequately predicts the flexural resistance at first yield in almost all cases that the axial load demand is constant. The first yield moment of specimens A4 and B4 is 30% larger than that predicted by the P-M interaction curve. This is because the P-M interaction curve does not depict the influence of axial load variation on the flexural resistance of these columns. Finally, specimen C4 (W14x82, P/P_y=0.75) also developed a higher flexural resistance than what is predicted by the P-M interaction curve. However, if the full length member was considered, then member (flexural) buckling could have been the primary instability mode in this case considering the high compressive axial load demand imposed on this column.

Vis-à-vis the above discussion, the P-M interaction curve according to the ANSI/AISC 360-16 provisions seems rational for predicting a beam-column's flexural resistance at first yield. However, this is not the case for the column's maximum attained moment (see Fig. 9b) regardless of the imposed compressive axial load demand. In particular, the P-M interaction curves were derived analytically considering beam-columns without acknowledging any hardening (i.e., elastic perfectly-plastic material assumption) (ASCE 1971; Bruneau et al. 2011). Figure 9b underscores the influence of the kinematic and isotropic hardening on M_{max}. This is more evident in columns with more compact cross-sections (Groups B and C), in which M_{max} is underestimated by at least 30% and 40%, respectively. The delay in the local buckling formation leads to an appreciable amount of cyclic hardening. This is not so apparent in steel columns with moderately ductile cross-sections (i.e., Group A) due to the early onset of geometric instabilities after flexural yielding. The general consensus is that a thorough re-assessment of the P-M interaction curves for steel beam-columns used in seismic applications shall be conducted, which agrees with recent related work (Zeimian et al. 2018). Such an assessment is outside the scope of the present paper.

Column Axial Shortening

Figure 6 shows the column axial shortening versus the corresponding column chord rotation. Previous studies (MacRae et al. 1990; Elkady and Lignos 2018a, b) found that axial shortening is strongly correlated with a steel column's cumulative inelastic rotation demands. Thus, specimens subjected to monotonic lateral loading (see Figs. 6a, 6d, 6g) exhibit only minor axial shortening of up to 30mm (i.e., 1.4% L) regardless of the cross-section web slenderness ratio and the imposed compressive axial load. In contrast, specimens subjected to symmetric cyclic lateral loading shorten by up to 110mm (6% L) due to the large number of inelastic drift cycles. The higher the web slenderness ratio the larger the column axial shortening because the column web becomes more susceptible to local buckling-induced softening.

Although specimen C4 was subjected to a P/P_y=0.75, it shortened more-or-less by the same amount with specimen C3 that was subjected to P/P_y=0.5 (see Fig. 6i versus Fig. 6h). This implies that the neutral-axis position of the cross-section strongly influences the corresponding column axial shortening. In particular, in the above two cases, due to the high compressive axial load, the neutral axis always remained outside the cross-section. As such, the cross-section's entire web experienced compressive stresses throughout the imposed lateral drift history. MacRae et al. (2009) found that the column axial shortening is practically not influenced by the applied compressive axial load if $P/P_y > A_w/A$ (in which, A_w and A are the web area and gross cross-section area, respectively). The experimental results suggest that this mechanistic assumption holds true for end steel MRF columns experiencing transient axial load demands if the imposed axial load ratio is still above the threshold value of A_w/A despite of the corresponding axial load variation range. In particular, referring to Figs. 6e and 6f, Specimens B3 (P/P_y=0.5) and B4 (P_g/P_y=0.5±P_v/P_y=0.25) are subjected to the same lateral drift histories but considerably different axial load demands. Nonetheless, they both experienced nearly the same axial shortening due to the aforementioned reason.

Effect of Transient Axial Load

Figure 10 shows the history of axial load ratio variation versus the column axial shortening, Δ_{axial}, for two specimens (A4 and B4). In order to quantify their axial stiffness deterioration, the instantaneous stiffnesses, K_{axial}^{-} and K_{axial}^{+}, corresponding to the beginning and the end of each lateral drift loading excursion, respectively, are extracted as illustrated in Figs. 10a and 10b. The $K_{axial}^{+/-}$ values are normalized with respect to the elastic axial stiffness, $K_{axial,el}$, of the respective column based on measured geometric and material properties (i.e., $K_{axial,el}=EA/L$). Accordingly, the normalized axial stiffness is shown Figs. 10c-d, for the first excursion of each drift level of the employed lateral loading protocol. In both cases, the axial stiffness deteriorates rapidly right after the onset of web and flange local buckling of column specimens A4 and B4. This is more evident in the negative loading direction once the compressive axial load reaches 75% P_y ($K_{axial}^{+}/K_{axial,el}$=54% and 34% for specimen A4 and B4, respectively). While the lateral drift progresses, the rate of axial stiffness degradation stabilizes until the axial load carrying capacity is lost (K_{axial}^{+}=0). This limit state is depicted relatively well in Fig. 10a for Specimen A4. On the other hand, Specimen B4 lost its axial load carrying capacity during the last lateral loading excursion as shown in Fig. 10b. To the best of the authors knowledge, the data presented herein is unique and can facilitate the calibration of mechanics-based numerical models that explicitly capture axial stiffness degradation as well as column axial shortening (Suzuki and Lignos 2017; Do and Filippou 2018; Kolwankar et al. 2018).

Plastic Hinge Length

Figure 11a shows the measured plastic hinge length, L_{PH}, for all the column specimens. The plastic hinge length is defined as the length between the column base plate and the last cross-sectional level experiencing plastic strains. The latter is deduced through linear interpolation between the strain gauges measurements. From this figure, the W14x61 and W16x89 specimens developed an L_{PH} of 1.6~2.0 *d*. The stockier W14x82 specimens developed a fairly large L_{PH} of 2.0~2.6 *d*. The spread of yielding at the column base relates to the steel material hardening (Kanno 2016) and the corresponding cross-section local slenderness ratio. In particular, if the onset of local buckling is delayed, then the spread of plasticity becomes large for mild steels exhibiting combined kinematic/isotropic hardening. This is the reason for the notable differences between the measured plastic hinge length between specimens in Group C and Groups A and B. While all three steel heats were nominally the same (i.e., A992 Gr. 50), the chemical composition of the Group C steel material includes a notably larger percentage of Manganese. As stated earlier, this influences the steel material hardenability (Shirasawa et al. 1981; Bruneau et al. 2011) and in turn the extent of plastic hinge length of a steel member.

Figure 11a suggests that the employed lateral loading protocol has a negligible effect on the column plastic hinge length (e.g. specimen B2 versus B3 and similarly C2 versus C3). On the other hand, the presence of high compressive axial load demands augments the plastic hinge length. The resultant second-order moment due to the compressive axial load pushes the center of local buckling further away from the column base, thereby increasing the associated plastic hinge length. This is schematically illustrated in Fig. 11b. In particular, specimens A2 and B2 (P/P_y=0.5) developed a 12% larger plastic hinge length compared to specimens A1 and B1 (P/P_y=0.3), respectively. Similarly, specimen C2 developed a plastic hinge length that is 30% larger than specimen C1. The above observations reflect the findings from prior related experimental studies (Nakashima et al. 1990; Peng et al. 2008; Suzuki and Lignos 2015a; Elkady and Lignos 2016).

Also superimposed in Fig. 11a is the predicted L_{PH} values based on the Elkady and Lignos (2018b) empirical model. This model was developed based on high-fidelity CFE simulations of steel columns under cyclic loading. In particular, the proposed empirical model relates L_{PH} to the web slenderness ratio, h/t_w, the member slenderness ratio, L_b/r_y, and the compressive axial load ratio, P/P_y. Although the empirical model predicts relatively well the plastic hinge length of Group A and B specimens, it underestimates L_{PH} by 40%, on average, for the Group C specimens. This is primarily related to the associated variability in material-hardening properties that is not captured by this empirical model. Notably, the observed plastic hinge lengths of Groups A and B are in a reasonable agreement with the minimum L_{PH} of 1.5 d specified in the New Zealand standards, NZS 3404 (SNZ 2007), for Category 1 and 2 members (equivalent to highly ductile members per ANSI/AISC 341-16).

Vis-à-vis the above discussion, the experimental results facilitate the identification of the potential plastic hinge length of a steel column for member stability verifications.

Section Classification and Scale Effects

In general, deep wide-flange steel columns (d > 400mm) are prone to geometric instabilities associated with local and/or lateral torsional buckling (NIST 2010b). In a recent testing program (Elkady and Lignos 2018a), the second and third authors tested a 4m long fixed-end column with a deep W24x146 cross-section under symmetric cyclic loading combined with a constant P/P_y=0.5. This specimen had a comparable web and flange local slenderness ratio with specimen C3 (W16x89) tested herein. The out-of-plane movement/rotation restraint in the full-scale and cantilever specimen was enforced by two actuators and flexurally-rigid steel beams, respectively. This was additionally checked using measurements from a wireless displacement tracking system. Strain and deformation measurements confirmed as well that the inflection point in the full-scale specimen remained at the column mid-height throughout the test (see Elkady and Lignos 2018a). Accordingly, the results from both specimens are directly comparable and the only differences in the measured response can be attributed to similitude; hence, the "deep-column" effect on the steel column stability can be properly characterized. Issues related to similitude for future experimental studies related to the seismic stability and ductility of steel columns can be highlighted. The predominant instability mode in both specimens was local buckling-induced softening followed by column axial shortening (Elkady and Lignos 2018a) as indicated in Figs. 12a and 12b. In particular, Fig. 12c shows a comparison of the normalized moment-rotation relations of the two specimens. Although both specimens reached to a comparable normalized peak moment, the W24x146 column experienced local buckling early on in the lateral loading history compared to the W16x89 steel column. This is attributed to the restraint that the flange provides to the web against local buckling. In particular, the web of the W24x146 cross-section is less restrained by the flanges against local buckling compared to the W16x89 cross-section. For the same reason, at any given drift following the onset local buckling, column axial shortening in the W24x146 column was about 2 times larger than that of the W16x89 column as shown in Fig. 12d. This simple comparison highlights the need to re-define the cross-sectional compactness limits in future design provisions by acknowledging the interaction between the web and flanges rather than treating those limits as an individual plate rule whereas the section classification limits are determined by comparing the most slender plate between the web and flange with the respective codified slenderness limits (Chen et al. 2013).

A side aspect to be thought through carefully is the proper scaling selection to characterize the hysteretic behavior of deep columns. Prior studies (Zargar et al. 2014) attempted to characterize the behavior of deep columns through relatively small-scale experiment. Although informative, the observed instability modes in these studies departed from the observed ones at full-scale. While lateral torsional buckling was observed in both cases, column axial shortening due to progression of column web buckling was not depicted at all due to similitude. Moreover, the damage progression, local and member instability synergistic action was not traced. Similar issues have been raised in fracture-related problems when fracture toughness is transferred from lab- to real-scale components (Pericoli and Kanvinde 2018).

Column Repairability Curves

The feasibility of conducting column repairs in the aftermath of earthquakes can be typically decided based on the extent of damage represented by the magnitude and size of the local buckling wave (FEMA 2009a). The experimental program discussed herein as well as prior physical testing of wide-flange steel columns (MacRae et al. 1990; Newell and Uang 2006; Suzuki and Lignos 2015b; Ozkula et al. 2017; Elkady and Lignos 2018a) highlight that steel columns may experience significant residual axial shortening. This could compromise the steel column repairability. Moreover, from a structural safety stand point, another compelling issue is the reserve capacity of a steel column after a mainshock. Reconnaissance reports indicate that aftershocks could often be quite damaging leading to structural collapse (Clifton et al. 2011; Okazaki et al. 2013).

In this regard, the concept of "Column Repairability Curve" is introduced herein to integrate all the aforementioned damage indicators into a single compact graphical format to facilitate the decision-making for steel column repair actions in the aftermath of earthquakes. Figure 13 shows such curves for different column specimens experiencing both asymmetric (see Figs. 13a, 13b) and symmetric local buckling (see Fig. 13c) near the column base. These curves combine three interdependent column performance indicators with the column lateral drift demand, θ. In particular, these indicators include the normalized residual flexural resistance of a steel column as a function of the peak flexural resistance, M_{max} (top horizontal axis); the corresponding column axial shortening, Δ_{axial} (right vertical axis); and the flange tip displacement, δ_f, indicating the local buckling wave amplitude (left vertical axis). This displacement is extracted from LED measurements shown in Fig. 7. Note that in the column repairability curves, axes are not in scale.

Referring to Figs. 13a and 13b, for columns experiencing asymmetric buckling, the corresponding flange tip displacement is almost double the column residual axial shortening. At lateral drift demands of 2% (representative of a design-basis earthquake), column repairability by means of straightening and/or strengthening the buckled region is feasible considering that both δ_f and Δ_{axial} are less than 10mm. Although the corresponding residual flexural resistance of these columns at a 2% drift demand is at least 70% M_{max}, this loss can be restored with the above repair measures. Referring to Fig. 13c, for columns experiencing symmetric local buckling, Δ_{axial} and δ_f are nearly the same. Due to the exponential increase of residual axial shortening, a column may practically be unrepairable after 2% radians. It is acknowledged that the repairability assessment is subject to an expert's opinion as well as the building characteristics and regional design practices. The column repairability curves presented herein are indicative and can provide a quantitative assessment of a steel column's damage state if the expected lateral drift demands can be somehow estimated. These curves can also be used as a tool to quickly estimate the lateral drift demands as well as the flexural resistance loss if physical measurements of the flange tip displacement and/or column residual shortening are conducted after an earthquake. Alternatively, one can utilize multivariate damage fragility functions such as those developed by Elkady et al. (2018). These functions relate pre-described levels of column residual strength and axial shortening (i.e., damage states), to the column's web slenderness, axial load demand and story-drift ratio demand.

Assessment of Nonlinear Modeling Recommendations for Wide Flange Steel Columns

PEER/ATC 72-1 Modeling Guidelines

PEER/ATC 72-1 (PEER/ATC 2010) provides engineering practice-oriented nonlinear modeling guidelines for structural steel components for the nonlinear seismic performance assessment of existing and prospective structural designs. These guidelines employ idealized concentrated plasticity component models for use in nonlinear static and response-history analyses of frame structures. These recommendations are largely based on physical testing of steel beams in fully restrained beam-to-column connections (FEMA 2000; Lignos and Krawinkler 2011). Due to lack of column test data at the time, it is common that the same recommendations are used for the nonlinear modeling of wide-flange steel columns. In particular, PEER/ATC 72-1 *Option 1* defines the input model parameters for the monotonic backbone curve of a steel structural component. This is treated as a unique property of the structural component and shall be used with hysteretic component models that explicitly simulate cyclic deterioration in strength and stiffness (Ibarra et al. 2005; Krawinkler 2009; Lignos and Krawinkler 2011). Alternatively, in order to conduct a nonlinear static analysis, PEER/ATC 72-1 *Option 3* modeling option is employed. This represents the first-cycle envelope curve of a structural component subjected to a symmetric cyclic lateral loading protocol. This curve, which is loading history dependent, only captures implicitly the influence of cyclic deterioration on a component's strength and stiffness. The above nonlinear modeling options are evaluated herein based on direct comparisons with the gathered experimental data. To facilitate the subsequent discussion, selected comparisons are established based on tests conducted under monotonic (see Figs. 14a and 14b) and cyclic lateral loading (see Figs. 14c, 14d).

Elastic Effective Stiffness, K_e

Referring to Fig. 14, the PEER/ATC 72-1 modeling guidelines tend to overestimate the elastic stiffness, K_e, of wide-flange steel columns because the contribution of the shear deformations is neglected in the K_e computation. In principle, a member's total lateral deformation can be expressed as $\delta_{total} = \delta_b\,(1+\beta)$ in which, δ_b is the flexural deformation; and β is the bending-to-shear stiffness ratio ($\beta = K_b/K_s$). For cantilever members, K_b and K_s are calculated as $3EI/L$ and GAL/α, respectively, where I is the moment-of-inertia about the strong-axis, G is the shear modulus and α is the cross section's shear coefficient as per Cowper (1966). For instance, when the shear stiffness is infinitely large (K_s=∞), β approaches zero implying no shear deformations. For the range of cross-sections summarized in Table 1, α was found to be about 0.25, which corresponds to a 25% increase of a column's elastic deformation. Figure 15 summarizes the ratio of the theoretically-computed stiffness to the measured one from 152 wide-flange steel column experiments (Popov et al. 1975; MacRae et al. 1990; Nakashima et al. 1990; Newell and Uang 2006; Cheng et al. 2013a; Cheng et al. 2013b; Suzuki and Lignos 2015b; Ozkula et al. 2017; Elkady and Lignos 2018a) including the test data presented herein. The figure shows that K_e is overestimated, on average, by 30% when shear deformations are neglected. Accordingly, it is recommended that shear deformations be considered when computing a wide-flange steel column's effective stiffness, K_e. The corresponding formula for estimating the elastic effective stiffness of energy-dissipative links in eccentrically braced frames would suffice for this purpose (Bech et al. 2015; Lignos et al. 2019).

Effective Yield Strength, M_y^*, and Capping Strength, M_{max},

The PEER/ATC 72-1 modeling *Options 1* and 3 compute the corresponding effective yield strength as M_y^*=1.1 $Z\,f_{ye}\,(1\text{-}P/P_y)$ where, Z is the cross-section plastic modulus about the strong-axis; and f_{ye} is the expected yield stress. The predicted M_y^* tends to underestimate the measured one as demonstrated in Fig. 14. This is attributed to (a) the axial load-bending interaction that is only considered approximately from the equation above; and (b) the corresponding material cyclic hardening that is inherently captured by the coefficient 1.1 (Lignos and Krawinkler 2011). The former can be easily noted from Figs. 14a and 14b representing specimens subjected to P/P_y = 30% and 50%. The latter is justified from a comparison of the first-cycle envelopes of nominally identical specimens subjected to a symmetric and a collapse-consistent lateral loading history as shown in Figs, 14c and 14d, respectively. In particular, due to the relatively small number of inelastic cycles prior to the onset of local buckling, cyclic hardening is not as pronounced as it is in the case of a symmetric cyclic lateral loading history. As such, the predicted M_y^* is nearly the same with the measured one (see Fig. 14d).

The PEER/ATC 72-1 modeling guidelines suggest a constant capping-to-effective-yield strength ratio, M_{max}/M_y^*, of 1.1 that depicts the effects of material hardening on the post-yield behavior of a structural steel component. Albeit this value is fairly constant for steel beams due to the absence of axial load demands (Lignos and Krawinkler 2011), the test data herein indicate that M_{max}/M_y^* varies from 1.1 to 1.7 for Group A and B specimens; and up to 2.4 for Group C specimens. In particular, Group B and C specimens involve cross-sections with fairly compact webs, thereby delaying the onset of local buckling which in turn translates into a relatively high hardening ratio, M_{max}/M_y^*=1.5. Accordingly, for nonlinear phenomenological component modeling, M_{max}/M_y^* shall be computed by considering the cross-sectional slenderness and the corresponding axial load demand (Lignos et al. 2019).

Pre- and post-peak Plastic Rotations

Figures 16a and 16b summarizes the pre- (θ_p) and post-peak (θ_{pc}) plastic rotations, respectively, of the 12 tested column specimens. These values are deduced based on idealized trilinear curves fitted to the monotonic backbone and first-cycle envelope curves of each column specimen. Superimposed in the same figures are the computed values based on the PEER/ATC 72-1 modeling guidelines (both *Options 1* and *3*). Although the test data highlight the dependence of the achieved plastic rotation capacities on the cross-sectional local slenderness ratios and the applied axial load demand, the predicted values depict the former but not the latter effect. As noted earlier, the PEER/ATC 72-1 *Option 1* equations were developed based on test data from steel beams (i.e., zero axial load). As such, the computed values tend to overestimate the measured ones based on monotonic loading by at least 20%, when $P/P_y > 0.3$ and/or the corresponding cross-sectional web slenderness, $h/t_w > 25$. With regards to column specimens subjected to symmetric cyclic lateral loading, *Option 3* systematically overestimates both θ_p and θ_{pc} values by at least 50%. Noteworthy stating that for Specimen A3, which was subjected to a collapse-consistent lateral loading history, the predicted θ_{pc} value was well correlated with the measured one. This suggests the need for more refined lateral loading protocols for component modeling and acceptance criteria of structural components (Suzuki and Lignos 2014; Maison and Speicher 2016).

Continuum Finite Element Modeling Recommendations for Wide-Flange Steel Columns

High-fidelity CFE models can be effectively utilized to simulate the onset and progression of geometric instabilities associated with local and/or lateral torsional buckling in wide-flange steel columns under monotonic and cyclic loading. A number of recommendations are available for this purpose in the literature (Newell and Uang 2006; Elkady and Lignos 2015a; Fogarty and El-Tawil 2015; Araújo et al. 2017; Elkady and Lignos 2018b) with conflicting conclusions. In particular, Elkady and Lignos (2015a, 2018b) and Fogarty and El-Tawil (2015) suggest that local and member geometric imperfections (GIs) are of equal importance to properly simulate the onset of geometric instabilities due to local and lateral torsional buckling along a steel column that utilizes slender cross-sections. Others suggest that GIs are only important for properly simulating the monotonic behavior of steel beam-columns but not the cyclic one (Araújo et al. 2017). A more recent study (Wu et al. 2018a) suggested that GIs shall not be used for modeling the hysteretic behavior of deep and slender steel columns such that pre-selected bifurcation paths can be avoided. In prior studies (Newell and Uang 2006), GIs were neglected but these were not deemed to be critical for simulating the hysteretic behavior of columns utilizing stocky cross-section profiles. This section clarifies several of the aforementioned concepts in an intrinsic effort to provide guidance for CFE nonlinear modeling of steel columns. For this purpose the commercial finite element software ABAQUS-FEA/CAE (2011) is utilized with the following assumptions; The large deformation simulations employ quadratic shell elements with reduced integration (S4R) that are deemed to adequately trace geometric instabilities (Elkady and Lignos 2015a, 2018b). Material nonlinearity is considered with the Von Mises yield surface and a multiaxial plasticity model (Voce 1948; Armstrong and Frederick 1966; Lemaitre and Chaboche 1975), which was calibrated to uniaxial cyclic coupon tests of (ASTM 2015) A992 Gr. 50 steel (Suzuki and Lignos 2017) of similar microstructure and chemical composition with the steel materials discussed herein. The material model parameters are loading history independent (Elkady and Lignos 2018b; Sousa and Lignos 2018). Two types of analyses are conducted with (w) and without (w/o) triggering local and member imperfections (GIs) based on conventional buckling analysis. The amplitude of local imperfections in the flanges and the web are set to $b_f/250$ and $h_w/250$, respectively, based on imperfection measurements conducted in prior testing programs (Elkady and Lignos 2016; Elkady and Lignos 2018a) for a similar range of cross-section profiles with the ones discussed herein. The above geometric imperfections are within the manufacturing limits of wide-flange products (ASTM 2014). Note that desired GIs shape and amplitude are achieved by scaling and superimposing the different local buckling modes of the column model. For more details, the reader is referred to Elkady and Lignos (2018b).

Figure 17 shows sample comparisons between the CFE predictions and the test data of representative specimens to address the above issues. Referring to Figs. 17a and 17b, the agreement between the simulated and measured responses is noteworthy when GIs are considered both for monotonic and cyclic lateral loading. The same figure also shows the simulated results when local GIs are not incorporated in the CFE model. The results suggest that the CFE simulation model in this case overestimates by at least a factor of two the flexural resistance and plastic deformation capacities of steel columns under monotonic and/or cyclic loading. These simple comparisons suggest that CFE simulation models shall (a) properly consider the combined kinematic/isotropic hardening of mild steels and (b) always incorporate GIs of proper magnitude to accurately trace the onset of local and/or lateral torsional buckling of steel wide-flange beam-columns. Recommendations developed by the second and third author (Elkady and Lignos 2018b) can facilitate this effort. These agree with recent modeling recommendations on how to model complex three-dimensional behavior of steel members (Zeimian et al. 2018).

Summary and conclusions

This paper discusses in detail the main findings from an experimental program that characterized the behavior of wide-flange steel columns under monotonic and reversed cyclic lateral loading coupled with high constant and variable axial load demands. The tests were conducted with 1800mm long cantilever test specimens. Test parameters included the cross-section local slenderness, the applied axial load ratio (constant versus variable) as well as the lateral loading history. The test program also offered the opportunity to assess the state-of-the-art recommendations for models of various computational resolutions including concentrated plasticity and high-fidelity continuum finite element (CFE) approaches.

The typical damage progression of the test specimens involved flexural yielding followed by cross-sectional local buckling regardless of the employed loading history. Due to the relatively small member slenderness, L_b/r_y, of the test specimens, global instabilities (i.e., lateral torsional and/or flexural buckling) were not evident at lateral drift amplitudes of up to 7% even at high axial load demands ($P/P_y > 0.5$). The local buckling mode was fairly symmetric in test specimens under symmetric lateral loading histories coupled with constant compressive axial load. On the other hand, wide-flange steel columns subjected to asymmetric lateral loading or variable axial load demands (that varies between compression and tension) developed an asymmetric local buckling mode. The plastic hinge region varies from 1.6 *d* to 2.5 *d* with the center of local buckling moving away from the column base with higher compressive loads. However, this becomes insensitive to the compressive axial load ratio if this becomes larger than a threshold equal to web-to-total cross-section area ratio.

Under monotonic lateral drift, the test results suggest that steel columns subjected to modest axial load demands ($P/P_y = 0.30$) attain a residual flexural strength due to stabilization of the developed cross-sectional local buckling length. On the other hand, steel columns under high axial load demands ($P/P_y \geq 0.5$) typically attain a secondary negative stiffness at large lateral deformations due to coupling of local and lateral torsional buckling. In any case, the loss of a column's axial load carrying capacity is accompanied by severe axial shortening.

Columns subjected to high axial load demands and reversed cyclic lateral loading deteriorate in flexural resistance rapidly after a reference lateral drift of 2%. In fact, most of the tested specimens lost their axial load carrying capacity at a lateral drift of 4%. Nonetheless, the test results underscore the influence of the imposed lateral loading history on the column's plastic deformation capacity. Although inconclusive, seismic acceptance criteria should eventually consider the cumulative plastic rotation demands in addition to a reference plastic deformation.

The hysteretic behavior of steel columns under variable axial load demands is highly asymmetric. The increased compressive axial load due to the transient effects causes local buckling initiation at the column flange experiencing the highest compressive stresses. In the opposite loading direction, the flexural resistance of the column is maintained to at least 80% of the maximum attained moment even at lateral drift demands of up to 4% due to local buckling straightening In this case, the experimental results shall be interpreted as lower bound responses because the imposed variable axial loading histories conservatively ignored the redistribution of axial forces within a steel frame building once its structural members enter into the inelastic regime. This issue deserves much attention in future experimental studies.

The ANSI/AISC 360-16 (AISC 2016b) axial load–bending (P-M) interaction curve predicts relatively well the first flexural yielding of all the test specimens. However, the peak column flexural resistances of the specimens were at least 30% larger than those predicted by the P-M interaction equation, regardless of the imposed axial load demand. This is due to the fact that this interaction curve does not acknowledge the post-yield hardening of typical mild steel materials (i.e., assumption of elastic-perfectly plastic material). This assumption seems to work well for steel columns utilizing moderately ductile cross-sections as per ANSI/AISC 341-16 (AISC 2016a) that develop a negligible amount of cyclic hardening due to the early occurrence of local buckling. At high compressive axial load demands ($P/P_y \geq 0.75$) the P-M interaction shall be carefully evaluated based on prospective tests with column specimens prone to member buckling.

The experimental data summarized herein also served for the validation of state-of-the-art component modeling guidelines (PEER/ATC 2010) widely used by the engineering profession for the seismic performance assessment of existing and prospective steel building designs. In particular, the PEER/ATC 72-1 *Option 1* and *3* component models were thoroughly assessed. The former defines the monotonic backbone curve of a structural component, while the latter defines its first-cycle envelope curve based on experiments conducted with standard symmetric cyclic lateral loading histories. In particular, both *Option 1* and *3* models tend to underestimate a column's elastic lateral stiffness by up to 30% when shear deformations are neglected. The effective flexural strength, M_y^*, is only predicted well for column specimens subjected to modest axial load demands of $0.30P_y$ representative of steel MRF columns. Although the post-yield hardening ratio, M_c/M_y^*, could range anywhere from 1.1 to 1.5 depending on the imposed axial load demand and the cross-sectional web local slenderness, the PEER/ATC 72-1 component models assume a constant value of 1.1, which is typical for steel beams (i.e., zero axial load ratio) with slender but seismically compact cross-sections (Lignos and Krawinkler 2011). Similarly, the PEER/ATC 72-1 *Option 1* model predicts reasonably well the monotonic backbone curve of wide-flange steel columns under modest axial load demands ($0.30P_y$) and whose web slenderness ratios are within the calibration range of the *Option 1* model ($20< h/t_w <55$). In cases that $P/P_y >0.30$

and h/t_w >25, the *Option 1* model over-predicts the corresponding pre- (θ_p) and post-capping (θ_{pc}) plastic rotation capacities by at least 20%. Although the ATC/PEER 72-1 *Option 3* model over-predicts the θ_p and θ_{pc} values by at least 50% for steel columns under reversed cyclic lateral loading, much closer predictions are obtained for columns under collapse-consistent lateral loading.

Continuum finite element (CFE) models shall always consider geometric imperfections (GIs) to properly trace local buckling of wide-flange steel columns with seismically compact cross-sections near the high ductility limits as per ANSI/AISC 341-16 (AISC 2016a). In particular, comparisons between the measured data and predictions from high-fidelity CFE column models indicate that if GIs are neglected, then the predicted local buckling initiation as well as the subsequent column damage progression is vastly different than that observed in reality. The modeling recommendations by Elkady and Lignos (2018b) are deemed rational for simulating cyclic plastic buckling of wide-flange steel columns.

The concept of a column repairability curve was also introduced. Based on the gathered experimental data, these curves integrate in a single compact graphical format various column performance indicators including the residual axial shortening, flange-tip in-plane deformation due to local buckling and the column reserve capacity as a function of the story-drift demand. In general, the column repairability curves presented herein indicate that when a column experiences 40mm flange-tip deformation (≈7° flange rotation angle) or 30mm residual axial shortening, its reserve capacity is less than 80% of the attained peak flexural resistance. In that respect, the interaction of a column with its concrete footing also affects the extent of column (Inamasu et al. 2017). This is outside the scope of the present study since the considered test specimens were idealized with a fixed end boundary condition.

Finally, comparisons of the gathered experimental results with those from prior related studies indicate that scale effects shall be carefully considered in order to properly trace the primary column instability mode. The interaction between a wide-flange cross-section's flange and web shall be considered to properly define section classification limits to control the axial shortening and the cyclic deterioration in flexural strength of steel columns for seismic applications.

Acknowledgements

This study was based on work supported by the Natural Sciences and Engineering Research Council of Canada (NSERC) under the Discovery Grant Program. The test specimen material and fabrication was generously donated by ADF Corporation Inc. Additional support for the second author was provided by the Swiss National Science Foundation (Award Number 200021_169248) as well as École Polytechnique Fédérale de Lausanne (EPFL). The financial support is gratefully acknowledged. The authors would like to sincerely thank Dr. William Cook, Mr. John Bartczak at Jamieson Structural Laboratory at McGill University as well as Prof. Colin Rogers for their invaluable assistance for the successful completion of the testing program. Any opinions, findings, and conclusions or recommendations expressed in this paper are those of the authors and do not necessarily reflect the views of sponsors.

Notation

The following symbols are used in this paper:

A = gross cross-section area;
A_w = web's cross-section area;
b_f = flange's width;
C_b = Lateral-torsional buckling modification factor (AISC 2016b);
d = column cross-section's depth;
E = measured modulus of elasticity of steel;
$f_{u,w}$, $f_{u,f}$ = measured ultimate stress of steel in the columns web and flange, respectively;
$f_{y\ mill}$ = measured yield stress of steel based on mill certificate;
$f_{y\ w}$, $f_{y,f}$ = measured yield stress of steel in the columns web and flange, respectively;
$f_{u\ mill}$ = measured ultimate stress of steel based on mill certificate;
f_{yn} = minimum specified (nominal) yield stress of steel (ASTM 2015);
G = measured shear modulus of steel;
h = web's height;
I = column cross-section's moment-of-inertia about the strong-axis;
$K_{axial,el}$ = column's elastic axial stiffness;
K_{axial}^{-} = column's axial stiffness in the negative loading direction;
K_{axial}^{+} = column's axial stiffness in the positive loading direction;
K_b = column's elastic flexural stiffness based on bending deformations;
K_e = column's elastic flexural stiffness;
K_s = column's elastic flexural stiffness based on shear deformations;

L = column’s clear length, L=1750mm;

L_b = column’s unbraced length, L_b=1750mm;

L_c = column’s effective length for buckling about the weak-axis, L_c=875mm;

L_{PH} = column’s measured plastic hinge length;

M = moment demand at the top surface of the column base;

M_c = available bending strength (AISC 2016b);

M_{max} = peak measured bending resistance;

M_p = full plastic bending strength based on measured geometric and material properties;

M_y^* = effective yield bending strength (PEER/ATC 2010);

P = applied load in the gravity direction;

P_c = available axial strength (AISC 2016b);

P_g = applied gravity load offset;

P_y = axial yield strength based on measured geometric and material properties;

r_y = radius of gyration about the cross-section’s weak-axis;

R_y = ratio of the expected yield stress to the specified minimum yield stress (AISC 2016a);

t_f = flange’s thickness;

t_w = web’s thickness;

Z = column cross-section’s plastic modulus about the strong-axis;

α = cross-section’s shear coefficient (Cowper 1966);

β = bending-to-shear stiffness ratio;

Δ_{axial} = column’s axial shortening in the gravity direction;

δ_f = in-plane flange tip displacement with respect to the undeformed position;

δ_{OP} = out-of-plane column displacement with respect to the undeformed position;

θ = column’s chord-rotation over its clear length;

θ_p = column’s pre-capping plastic rotation capacity;

θ_{pc} = column’s post-capping plastic rotation capacity;

λ_{hd} = Limiting slenderness parameter for highly ductile compression elements (AISC 2016a);

ϕ = resistance factor (AISC 2016b).

References

ABAQUS-FEA/CAE. (2011). Dassault Systemes Simulia Corp., RI, USA. © Dassault Systèmes, 2010.

AISC (2016a). "Seismic provisions for structural steel buildings." *ANSI/AISC 341-16*, Chicago, .IL

AISC (2016b). "Specification for structural steel buildings ".*ANSI/AISC 360-16*, Chicago, .IL

Akcelyan, S., and Lignos, D. G. (2018). "Seismic retrofit of steel tall buildings with bilinear oil dampers." *Proc., 16th European Conf. on Earthquake Eng.*, Thessaloniki, Greece.

Araújo, M., Macedo, L., and Castro, J. M. (2017). "Evaluation of the rotation capacity limits of steel members defined in EC8-3." *J. of Constructional Steel Research*, 135, 11-29. DOI: 10.1016/j.jcsr.2017.04.004.

Alavi, B., and Krawinkler, H. (2004). "Behavior of moment- resisting frame structures subjected to near- fault ground motions." *Earthquake Eng. & Structural Dynamics*, 33(6), 687-706. DOI: 10.1002/eqe.369.

Armstrong, P. J., and Frederick, C. O. (1966). "A mathematical representation of the multiaxial bauschinger effect." *Materials at High Temperatures*, 24(1), 1-26. DOI: 10.1179/096034007X207589.

ASCE (1971). "Plastic design in steel, a guide and commentary." *Manual of Practice No. 41*, New York, USA.

ASCE (2014). "Seismic evaluation and retrofit of existing buildings." *ASCE/SEI 41-13*, Reston, VA.

ASTM (2014). "Standard specification for general requirements for rolled structural steel bars, plates, shapes, and sheet piling." *ASTM A6/A6M*-14, ASTM International, West Conshohocken, PA, USA.

ASTM (2015). "Standard specification for structural steel shapes." *ASTM A992/A992M*, ASTM International, West Conshohocken, PA, USA.

AWS (2009). "Structural welding code - seismic supplement." *AWS D1.8/D1.8M:2009*, Miami, Fl, USA.

Bech, D., Tremayne, B., and Houston, J. (2015). "Proposed changes to steel column evaluation criteria for existing buildings." *Proc., 2nd ATC-SEI Conf. on Improving the Seismic Performance of Existing Building and Other Structures*, San Francisco, CA, USA.

Bruneau, M., Uang, C.-M., and Sabelli, S. R. (2011). *Ductile design of steel structures*, McGraw Hill Professional.

Chen, Y., Cheng, X., and Nethercot, D. A. (2013). "An overview study on cross-section classification of steel H-sections." *J. of Constructional Steel Research*, 80, 386-393. DOI: 10.1016/j.jcsr.2012.10.006.

Cheng, X., Chen, Y., and Nethercot, D. A. (2013a). "Experimental study on H-shaped steel beam-columns with large width-thickness ratios under cyclic bending about weak-axis." *Eng. Structures*, 49, 264-274. DOI: 10.1016/j.engstruct.2012.10.035.

Cheng, X., Chen, Y., and Pan, L. (2013b). "Experimental study on steel beam–bolumns composed of slender H-sections under cyclic bending." *J. of Constructional Steel Research*, 88, 279-288. DOI: 10.1016/j.jcsr.2013.05.020.

Clark, P., Frank, K., Krawinkler, H., and Shaw, R. (1997). "Protocol for fabrication, inspection, testing, and documentation of beam-column connection tests and other experimental specimens”. *Report no. SAC/BD-97*. SAC Joint Venture, Sacramento, CA.

Clifton, C., Bruneau, M., MacRae, G., Leon, R., and Fussell, A. (2011). "Steel structures damage from the Christchurch earthquake series of 2010 and 2011." *Bulletin of the New Zealand Society for Earthquake Eng.,* 44(4), 297-318.

Cowper, G. R. (1966). "The shear coefficient in timoshenko’s beam theory." *Journal of Applied Mechanics*, 33(2), 335-340, DOI: 10.1115/1.3625046

Do, T. N., and Filippou, F. C. (2018). "A damage model for structures with degrading response." *Earthquake Eng. & Structural Dynamics*, 47(2), 311-332. DOI: 10.1002/eqe.2952.

Elkady, A., Ghimire, S., and Lignos, D. G. (2018). "Fragility curves for wide-flange steel columns and implications on building-specific earthquake-induced loss assessment." *Earthquake Spectra*. DOI: 10.1193/122017EQS260M.

Elkady, A., and Lignos, D. G. (2014). "Modeling of the composite action in fully restrained beam-to-column connections: l y of steeimplications in the seismic design and collapse capacit *E* ".special moment frames*arthquake Eng. & Structural Dynamics*, 43(13), 1935-1954. DOI: 10.1002/eqe.2430.

Elkady, A., and Lignos, D. G. (2015a). "Analytical investigation of the cyclic behavior and plastic hinge formation in deep wide-flange steel beam-columns." *Bulletin Earthquake Eng*, 13(4), 1097-1118. DOI: 10.1007/s10518-014-9640-y.

Elkady, A., and Lignos, D. G. (2015b). "Effect of gravity framing on the overstrength and collapse capacity of steel frame buildings with perimeter special moment frames." *Earthquake Eng. & Structural Dynamics*, 44(8), 1289–1307. DOI: 10.1002/eqe.2519.

Elkady, A., and Lignos, D. G. (2016). "Dynamic stability of deep and slender wide-flange steel columns-full scale experiments." *Proc. of the Annual Stability Conf.,* Orlando, Florida.

Elkady, A., and Lignos, D. G. (2018a). "Full-scale testing of deep wide-flange steel columns under multi-axis cyclic loading: Loading sequence, boundary effects and out-of-plane brace force demands." *ASCE J. of Structural Eng.*, 144(2). DOI: 10.1061/(ASCE)ST.1943-541X.0001937.

Elkady, A., and Lignos, D. G. (2018b). "Improved seismic design and nonlinear modeling recommendations for wide-flange steel columns." *ASCE J. of Structural Eng.*, 144(9). DOI: 10.1061/(ASCE)ST.1943-541X.0002166.

FEMA (2000). "State of the art report on connection performance." *Report FEMA-355D*, Federal Emergency Management Agency, Washington, DC.

FEMA (2009a). "Fragility curves for components of steel SMF systems." *Background Document FEMA P-58/BD-3.8.3*, Federal Emergency Management Agency, Washington, DC.

FEMA (2009b). "Quantification of building seismic performance factors." *Report FEMA-P695*, Federal Emergency Management Agency, Washington, DC.

Fogarty, J., and El-Tawil, S. (2015). "Collapse resistance of steel columns under combined axial and lateral loading." *J. of Structural Eng.*, 142(1). DOI: 10.1061/(ASCE)ST.1943-541X.0001350.

Gupta, A., and Krawinkler, H. (2000). "Behavior of ductile SMRFs at various seismic hazard levels." *J. of Structural Eng.*, 126(1), 98-107. DOI: 10.1061/(ASCE)0733-9445(2000)126:1(98).

Hamburger, R., Deierlein, G. G., Lehman, D. E., Lignos, D. G., Lowes, L. N., Pekelnicky, R., Shing, P. B., Somers, P., and van de Lindt, J. W. (2018). "Recommended modeling parameters and acceptance criteria for nonlinear analysis in support of seismic evaluation, retrofit, and design." *NIST GCR 17-917-45*, Prepared for the U.S. Department of Commerce and the National Institute of Standards and Technology (NIST) by the Applied Technology Council (ATC).

Haselton, C. B., Liel, A. B., Lange, S. T., and Deierlein, G. G. (2008). "Beam-column element model calibrated for predicting flexural response leading to global collapse of RC frame buildings." *Report No. 2007/03*, Pacific Earthquake Eng. Research Center, Berkeley, CA, USA.

Ibarra, L., and Krawinkler, H. (2005). "Global collapse of frame structures under seismic excitations." *Report No. 152*, The John A. Blume Earthquake Eng. Center, Stanford University, California, USA.

Ibarra, L. F., Medina, R. A., and Krawinkler, H. (2005). "Hysteretic models that incorporate strength and stiffness deterioration." *Earthquake Eng. & Structural Dynamics*, 34(12), 1489-1511. DOI: 10.1002/eqe.495.

Inamasu, H., Lignos, D. G., and Kanvinde, A. (2017). "Effect of column base flexibility on the hysteretic response of wide-flange steel columns." *Proc., 3rd Huixian Int. Forum on Earthquake Eng. for Young Researchers*, Urbana-Champaign, Illinois, USA.

Kanno, R. (2016). "Advances in steel materials for innovative and elegant steel structures in Japan-a review." *Structural Eng. Int.*, 26(3), 242-253. DOI: 10.2749/101686616X14555428759361.

Kolwankar, S., Kanvinde, A., Kenawy, M., Lignos, D. G., and Kunnath, S. K. (2018). "Simulating local buckling-induced softening in steel members using an equivalent nonlocal material model in displacement-based fiber elements." *J. of Structural Eng.*, 144(10), 04018192. DOI: 10.1061/(ASCE)ST.1943-541X.0002189.

Krawinkler, H. (2009). "Loading histories for cyclic tests in support of performance assessment of structural components." *Proc., 3rd Int. Conf. on Advances in Experimental Structural Eng.*, San Francisco, CA, USA, 15-16.

Krawinkler, H., Zohrei, M., Lashkari-Irvani, B., Cofie, N. G., and Hadidi-Tamjed, H. (1983). "Recommendations for experimental studies on the seismic behavior of steel components and materials." *Report No. 61*, The John A. Blume Earthquake Eng. Center, Stanford University, California, USA.

LATBSDC (2017). "An alternative procedure for the analysis and design of tall buildings located in the los angeles region."Los Angeles, CA, USA.

Lemaitre, J., and Chaboche, J. (1975). "A non-linear model of creep-fatigue damage cumulation and interaction (for hot metallic structures)." *Mechanics of visco-elastic media and bodies*.

Lignos, D., Krawinkler, H., and Whittaker, A. (2011a). "Prediction and validation of sidesway collapse of two scale models of a 4-story steel moment frame." *Earthquake Eng. & Structural Dynamics*, 40(7), 807-825, DOI: 10.1002/eqe.1061.

Lignos, D. G., Chung, Y., Nagae, T., and Nakashima, M. (2011b). "Numerical and experimental evaluation of seismic capacity of high-rise steel buildings subjected to long duration earthquakes." *Computers & Structures*, 89(11), 959-967, DOI: 10.1016/j.compstruc.2011.01.017.

Lignos, D. G., Hartloper, A., Elkady, A., Hamburger, R., and Deierlein, G. G. (2019). "Proposed updates to the ASCE 41 nonlinear modeling parameters for wide-flange steel columns in support of performance-based seismic engineering." *J. of Structural Eng.* (accepted).

Lignos, D. G., Hikino, T., Matsuoka, Y., and Nakashima, M. (2013). "Collapse assessment of steel moment frames based on E-Defense full-scale shake table collapse tests." *J. of Structural Eng.*, 139(1), 120-132. DOI: 10.1061/(ASCE)ST.1943-541X.0000608.

Lignos, D. G., and Krawinkler, H. (2011). "Deterioration modeling of steel components in support of collapse prediction of steel moment frames under earthquake loading." *J. of Structural Eng.*, 137(11), 1291-1302. DOI: 10.1061/(ASCE)ST.1943-541X.0000376.

Lignos, D. G., and Krawinkler, H. (2013). "Development and utilization of structural component databases for performance-based earthquake engineering." *J. of Structural Eng.*, 139(8), 1382-1394. DOI: 10.1061/(ASCE)ST.1943-541X.0000646.

MacRae, G. A., Carr, A. J., and Walpole, W. R. (1990). "The seismic response of steel frames." *Report No. 90-6*, Department of Civil Eng., University of Canterbury, New Zealand.

MacRae, G. A., Urmson, C. R., Walpole, W. R., Moss, P., Hyde, K., and Clifton, C. (2009). "Axial shortening of steel columns in buildings subjected to earthquakes." *Bulletin of the New Zealand Society for Earthquake Eng.*, 42(4), 275.

Maison, B. F., and Speicher, M. S. (2016). "Loading Protocols for ASCE 41 Backbone Curves." *Earthquake Spectra*, 32(4), 2513-2532. DOI: 10.1193/010816EQS007EP.

Miyamura, T., Yamashita, T., Akiba, H., and Ohsaki, M. (2015). "Dynamic FE simulation of four-story steel frame modeled by solid elements and its validation using results of full-scale shake-table test." *Earthquake Eng. & Structural Dynamics*, 44(9), 1449-1469. DOI: 10.1002/eqe.2526.

Nakashima, M., Nagae, T., Enokida, R., and Kajiwara, K. (2018). "Experiences, accomplishments, lessons, and challenges of E-Defense tests using world's largest shaking table." *Japan Architectural Review*, 1(1), 4-17. DOI: 10.1002/2475-8876.10020.

Nakashima, M., Takanashi, K., and Kato, H. (1990). "Test of steel beam-columns subject to sidesway." *J. of Structural Eng.*, 116(9), 2516-2531. DOI: 10.1061/(ASCE)0733-9445(1990)116:9(2516).

Newell, J. D., and Uang, C.-M. (2006). "Cyclic behavior of steel columns with combined high axial load and drift demand." *Report No. SSRP-06/22*, Department of Structural Eng., University of California, San Diego.

NIST (2010a). "Evaluation of the FEMA P695 methadology for quantification of building seismic performance factors." *NIST GCR 10-917-8*, NEHRP consultants Joint Venture.

NIST (2010b). "Research plan for the study of seismic behaviour and design of deep slender wide flange structural steel beam-column members." *NIST GCR 11-917-13*, NEHRP consultants Joint Venture.

Okazaki, T., Lignos, D. G., Midorikawa, M., Ricles, J. M., and Love, J. (2013). "Damage to steel buildings observed after the 2011 Tohoku-Oki earthquake." *Earthquake Spectra*, 29(S1), S219-S243. DOI: 10.1193/1.4000124.

Ozkula, G., Harris, J., and Uang, C. M. (2017). "Observations from cyclic tests on deep, wide-flange beam-columns." *AISC Eng. J.*, 54(1), 45-61.

PEER (2017). "Guidelines for performance-based seismic design of tall buildings." *Report No. 2017/06*, Pacific Earthquake Eng. Center, Berkeley, California, USA.

PEER/ATC (2010). "Modeling and acceptance criteria for seismic design and analysis of tall buildings." *PEER/ATC 72-1*, Redwood City, CA.

Peng, B. H., MacRae, G. A., Walpole, W. R., Moss, P., Dhakal, R., and Clifton, C. (2008). "Plastic hinge location in columns of steel frames subjected to seismic actions." *Bulletin of the New Zealand Society for Earthquake Eng.*, 41(1).

Pericoli, V., and Kanvinde, A. (2018). "Theoretical study of ductile fracture in steel structures in the presence of spatial variability in toughness." *J. of Structural Eng.*, 144(5), 04018024, DOI: 10.1061/(ASCE)ST.1943-541X.0002008.

Popov, E. P., Bertero, V. V., and Chandramouli, S. (1975). "Hysteretic behavior of steel columns." *Report No. EERC 75-11*, Earthquake Engineering Research Center, Berkeley, CA, USA.

Shirasawa, H., Kobayashi, H., and Jizaimaru, J. (1981). "The effect of various strengthening methods on ductility of high strength steel sheets." *Tetsu-to-Hagane (J. of the Iron and Steel Institute of Japan)*, 67(14), 2208-2215.

SNZ (2007). "Steel structures standard." *NZS 3404:2007*, Wellington, New Zealand.

Sousa, A. A., and Lignos, D. G. (2018). "On the inverse problem of classic nonlinear plasticity models." *EPFL-REPORT-231968*, Ecole Polytechnique Federale de Lausanne (EPFL), Lausanne, Switzerland.

Stoakes, C. D., and Fahnestock, L. A. (2016). "Strong-axis stability of wide flange steel columns in the presence of weak-axis flexure." *J. of Structural Eng.*, 142(5), DOI: 10.1061/(ASCE)ST.1943-541X.0001448.

Suzuki, Y., and Lignos, D. G. (2014). "Development of loading protocols for experimental testing of steel columns subjected to combined high axial load and lateral drift demands near collapse." *Proc. of the 10th National Conf. on Earthquake Eng.*, Anchorage, Alaska, USA.

Suzuki, Y., and Lignos, D. G. (2015a). "Large scale collapse experiments of wide-flange steel beam-columns." *Proc. of the 8th Int. Conf. on Behavior of Steel Structures in Seismic Areas,* Shanghai, China.

Suzuki, Y., and Lignos, D. G. (2017). "Collapse behavior of steel columns as part of steel frame buildings: Experiments and numerical models." *Proc., 16th World Conf. on Earthquake Eng.*, Santiago, Chile.

Tirca, L., Chen, L., and Tremblay, R. (2015). "Assessing collapse safety of cbf buildings subjected to crustal and subduction earthquakes." *J. of Constructional Steel Research*, 115, 47-61. DOI: 10.1016/j.jcsr.2015.07.025.

Toutant, G., Minouei, Y. B., Imanpour, A., Koboevic, S., and Tremblay, R. (2017). "Stability of steel columns in steel concentrically braced frames subjected to seismic loading." *Proc., ASCE Structures Congress*, Denver, Colorado, USA.

Uang, C.-M., and Bruneau, M. (2018). "State-of-the-art review on seismic design of steel structures." *J. of Structural Eng.*, 144(4), 03118002. DOI: 10.1061/(ASCE)ST.1943-541X.0001973.

Voce, E. (1948). "The relationship between dtress and strain for homogeneous deformation." *J. of the Institute of Metals*, 74, 537-562.

Wu, T.-Y., El-Tawil, S., and McCormick, J. (2018a). "Seismic collapse response of steel moment frames with deep columns." *J. of Structural Eng.*, 144(9), 04018145. DOI: 10.1061/(ASCE)ST.1943-541X.0002150.

Wu, T.-Y., El-Tawil, S., and McCormick, J. (2018b). "Highly ductile limits for deep steel columns." *J. of Structural Eng.*, 144(4), 04018016. DOI: 10.1061/(ASCE)ST.1943-541X.0002002.

Zargar, S., Medina, R. A., and Miranda, E. (2014). "Cyclic behavior of deep steel columns subjected to large drifts, rotations, and axial loads." *Proc., 10th National Conf. on Earthquake Eng.*, Anchorage, AK, USA.

Zeimian, R. D., Abreu, J. C. B., Denavit, M. D., and Denavit, T.-J. L. (2018). "Three-Dimensional Benchmark Problems for Design by Advanced Analysis: Impact of Twist." *J. of Structural Eng.* 144(12), 04018220. DOI: 10.1061/(ASCE)ST.1943-541X.0002224.

Table 1. Test matrix summary and measured geometric and material properties.

Spec. ID	Cross-Section	Lateral protocol	$\frac{P}{P_y}$	$\frac{b_f}{2t_f}$	$\frac{h}{t_w}$	$\frac{L_b}{r_y}$	Measured material properties [MPa]						
							E	$f_{y,mill}$	$f_{u,mill}$	$f_{y,w}$	$f_{y,f}$	$f_{u,w}$	$f_{u,f}$
A1	W14x61	Monotonic	30%	7.8	30.4	29.3	202315	384	493	374	358	471	478
A2	W14x61	Monotonic	50%										
A3	W14x61	Collapse-consistent	50%										
A4	W14x61	Symmetric	30%±45%										
B1	W16x89	Monotonic	30%	5.9	25.9	28.9	199402	379	514	383	368	491	497
B2	W16x89	Monotonic	50%										
B3	W16x89	Symmetric	50%										
B4	W16x89	Symmetric	50%±25%										
C1	W14x82	Monotonic	30%	5.9	22.4	29.0	199873	379	539	411	383	531	537
C2	W14x82	Monotonic	50%										
C3	W14x82	Symmetric	50%										
C4	W14x82	Symmetric	75%										

Table 2. Chemical composition of the steel material for Groups A, B and C [% mass].

Group	C	Mn	P	S	Si	Cu	NI	Cr	Mo	V	Cb	Sn
A	0.070	0.990	0.013	0.032	0.200	0.320	0.150	0.140	0.032	0.004	0.004	0.013
B	0.090	1.210	0.020	0.035	0.290	0.340	0.110	0.110	0.030	0.000	0.022	0.350
C	0.090	1.390	0.021	0.028	0.290	0.260	0.100	0.150	0.030	0.010	0.026	0.010

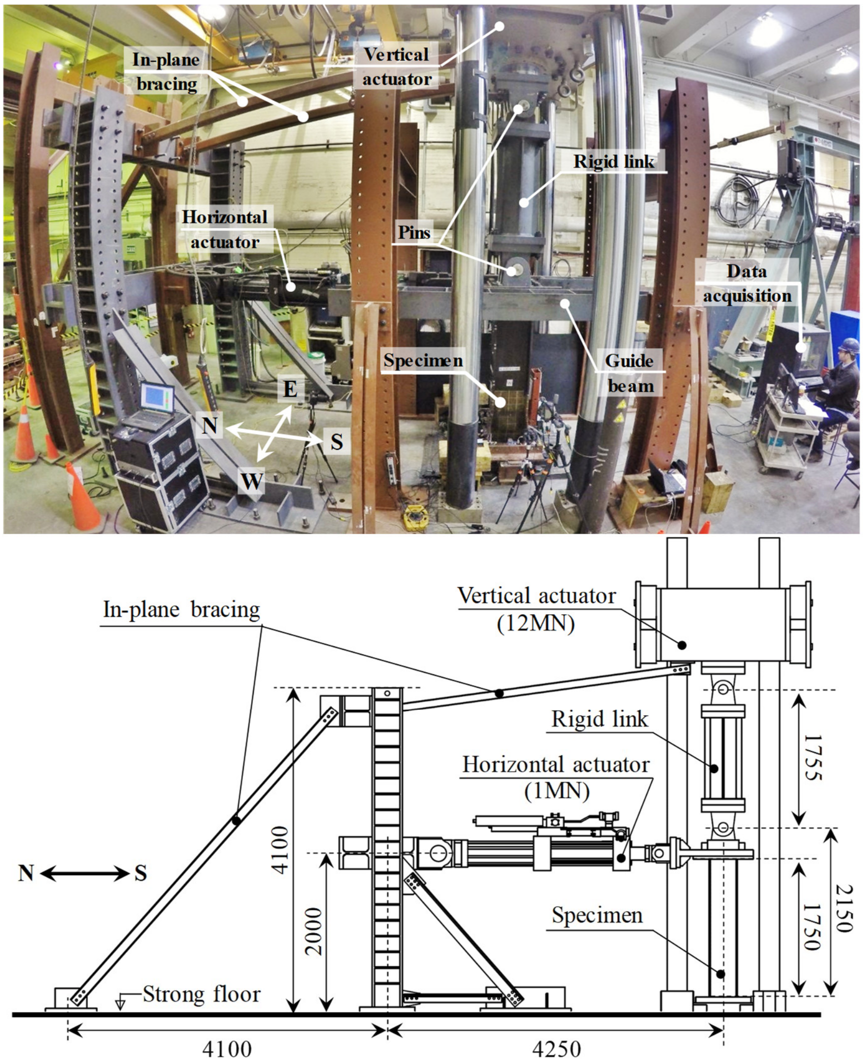

Fig. 1. Overview of the test setup for experimental testing of cantilever steel column specimens [Dimensions in mm].

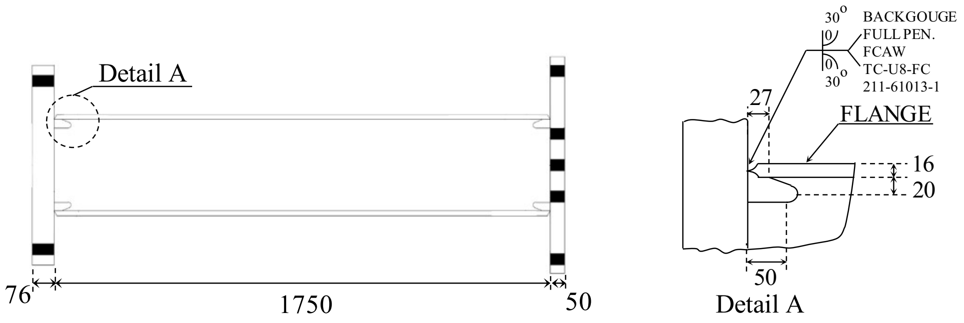

Fig. 2. Typical column specimen detail (Group A) [Dimensions in mm].

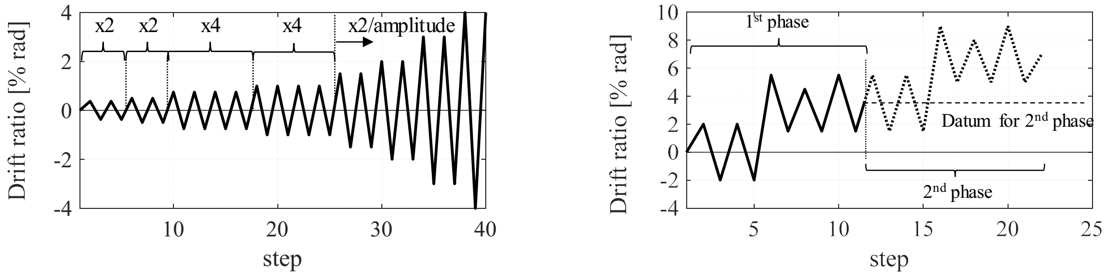

(a) Symmetric cyclic lateral loading protocol (b) Collapse-consistent lateral loading protocol

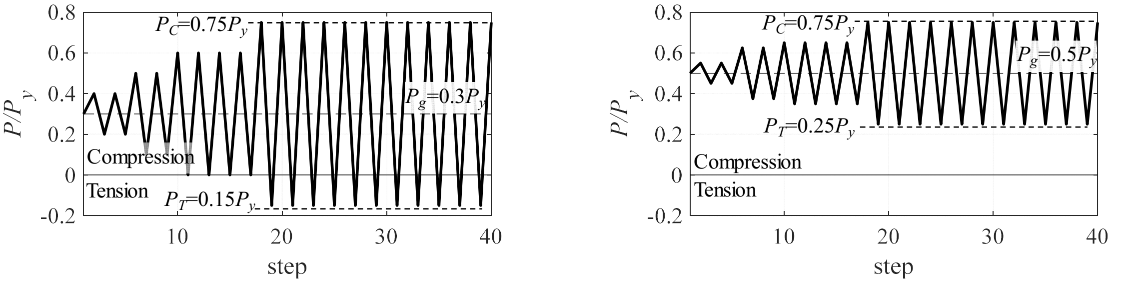

(c) Varying axial loading protocol P_g/P_y=30%±P_v/P_y=45%

(d) Varying axial loading protocol P_g/P_y=50%±P_v/P_y=25%

Fig. 3. Employed loading protocols for experimental testing of steel columns.

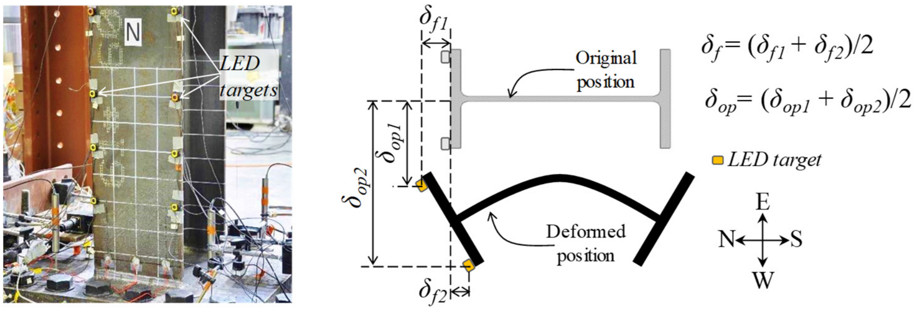

Fig. 4. Illustration of deduced out-of-plane column deformation and in-plane flange deformation based on LED measurements.

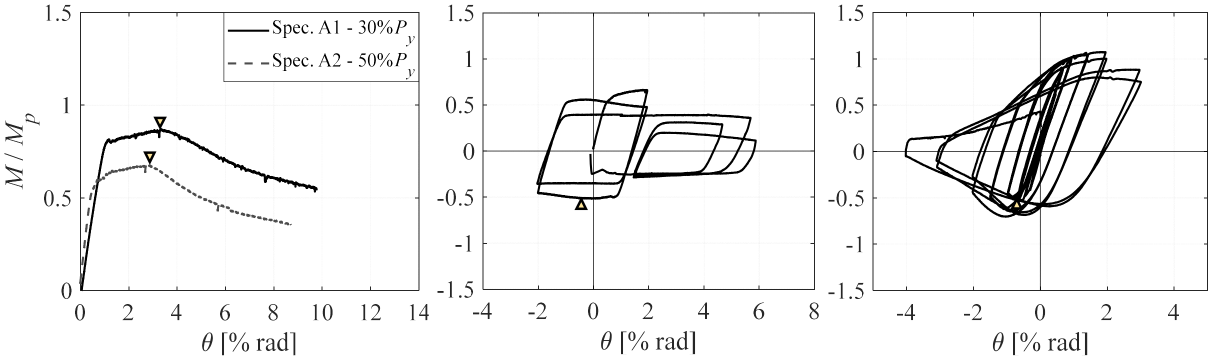

(a) Specimens A1 and A2 (W14x61) (Monotonic)

(b) Specimen A3 (W14x61) (Collapse-consistent - $P/P_y = 50\%$)

(c) Specimen A4 (W14x61) (Symm. - $P_g/P_y=30\%\pm P_v/P_y=45\%$)

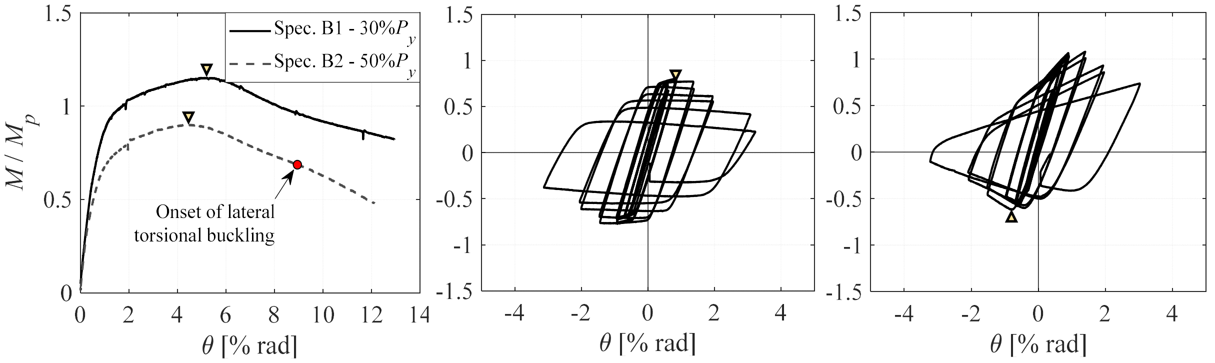

(d) Specimens B1 and B2 (W16x89) (Monotonic)

(e) Specimen B3 (W16x89) (Symm. - $P/P_y = 50\%$)

(f) Specimen B4 (W16x89) (Symm. - $P_g/P_y=50\%\pm P_v/P_y=25\%$)

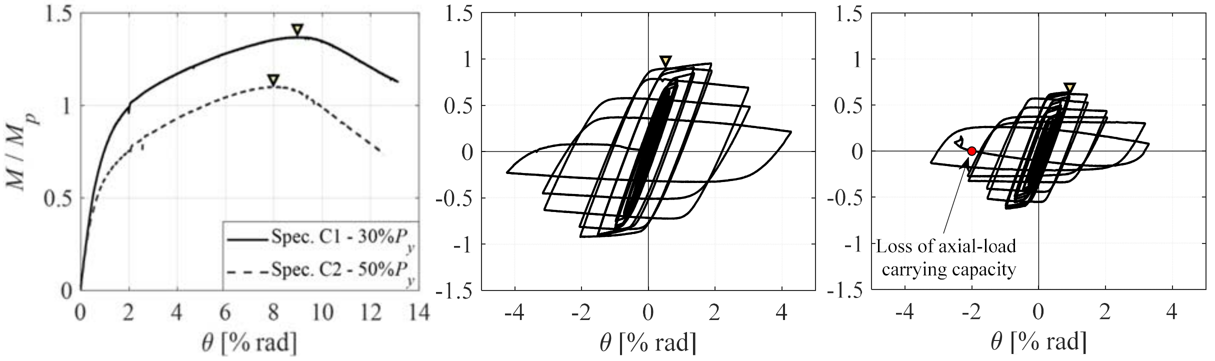

(g) Specimens C1 and C2 (W14x82) (Monotonic)

(h) Specimen C3 (W14x82) (Symm. - $P/P_y = 50\%$)

(i) Specimen C4 (W14x82) (Symm. - $P/P_y = 75\%$)

Fig. 5. End moment versus chord-rotation relation of tested specimens [triangular markers indicate onset of local buckling].

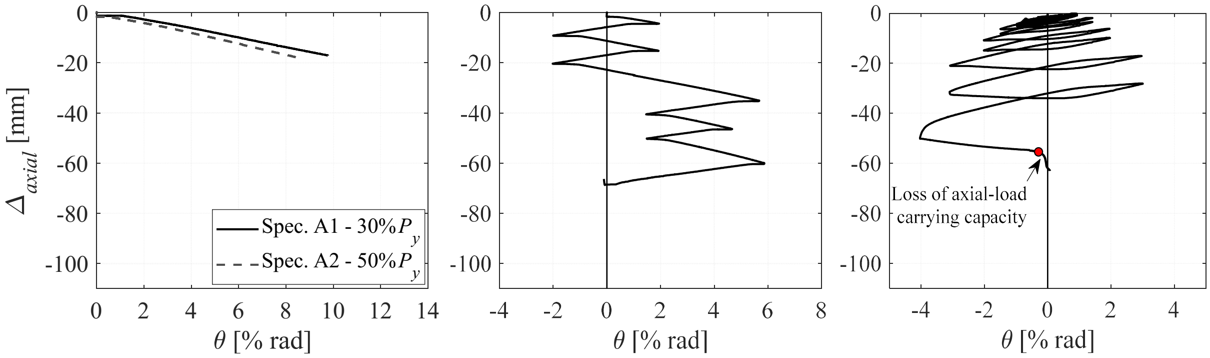

(a) Specimens A1 and A2 (W14x61)
(Monotonic)

(b) Specimen A3 (W14x61)
(Collapse-consistent – $P/P_y = 50\%$)

(c) Specimen A4 (W14x61)
(Symm. - P_g/P_y=30%±P_v/P_y=45%)

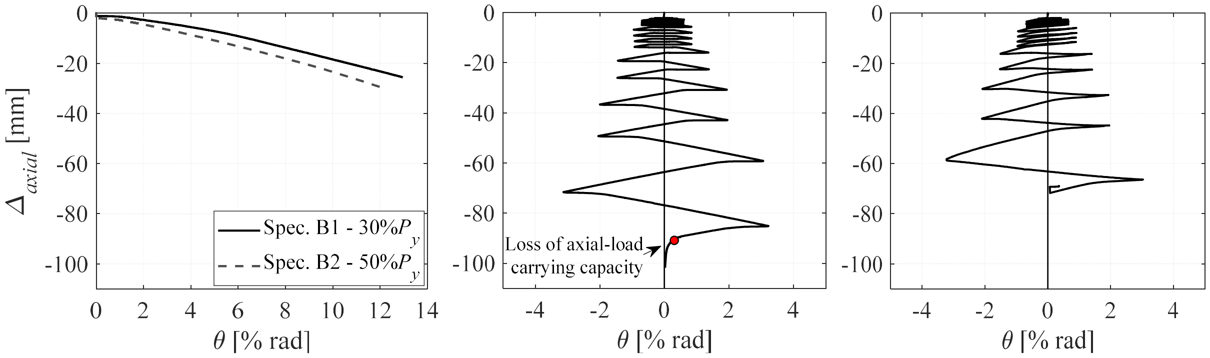

(d) Specimens B1 and B2 (W16x89)
(Monotonic)

(e) Specimen B3 (W16x89)
(Symm. cyclic - $P/P_y = 50\%$)

(f) Specimen B4 (W16x89)
(Symm. - P_g/P_y=50%±P_v/P_y=25%)

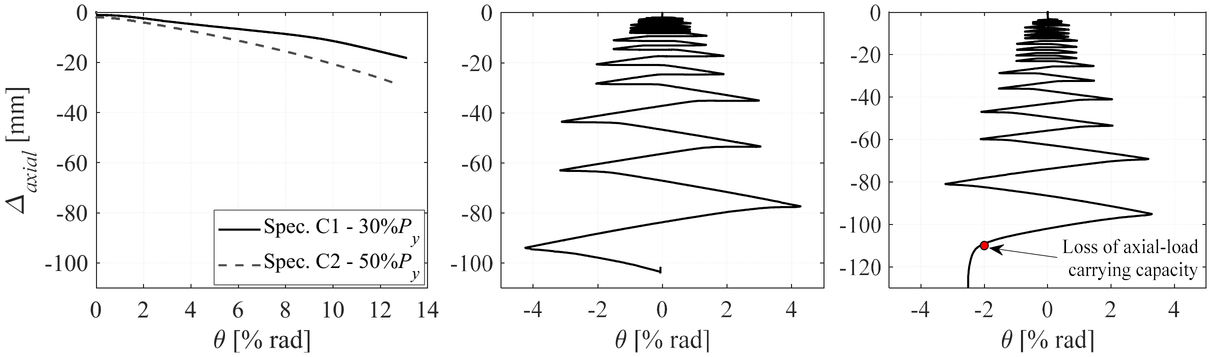

(g) Specimens C1 and C2 (W14x82)
(Monotonic)

(h) Specimen C3 (W14x82)
(Symm. cyclic - $P/P_y = 50\%$)

(i) Specimen C4 (W14x82)
(Symm. - $P/P_y = 75\%$)

Fig. 6. Column axial shortening versus chord-rotation relation of tested specimens.

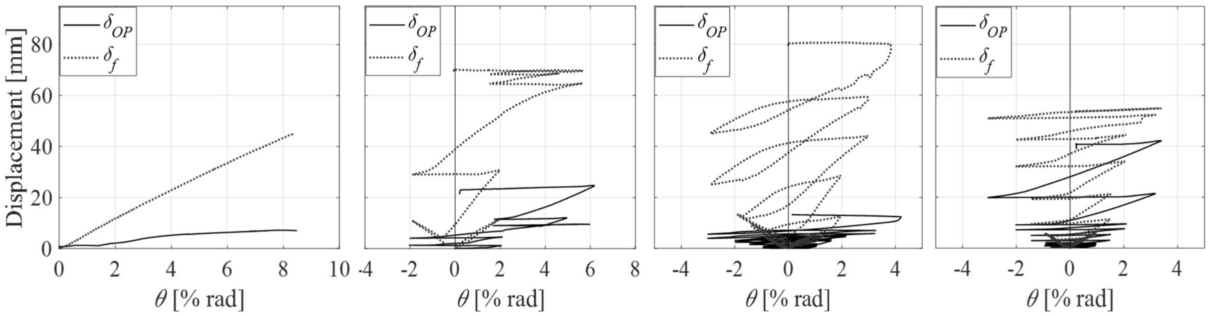

(a) Specimen A2 (W14x61)
(Monotonic + 50%P_y)

(b) Specimen A3 (W14x61)
(Collapse-cons. + 50%P_y)

(c) Specimen A4
(W14x61)
(Symm. + 30%± 45%P_y)

(d) Specimen B3
(W16x89)
(Symm. + 50%P_y)

Fig. 7. Out-of-plane and flange tip displacements versus chord-rotation of selected specimens.

(a) Yeilding (Monotonic + 50%P_y)

(b) LB* (Collapse cons.+50%P_y)

(c) Symm. LB* (Symm.+50%P_y)

(d) Double wave LB* (Symm.+50%P_y)

(e) Asymm. LB* (Symm.+30% ±45%P_y)

(f) Loss of axial load-carrying capacity (Symm.+75%P_y)

Fig. 8. Typical damage progression and geometric instability modes [*LB: Local buckling].

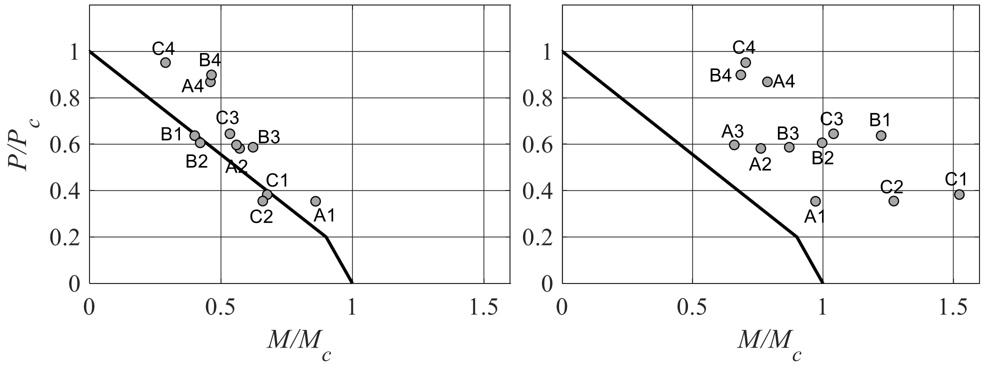

(a) data points at first-yield (b) data points at peak moment

Fig. 9. Evaluation of ANSI/AISC 360-16 axial force-bending (P-M) interaction curve.

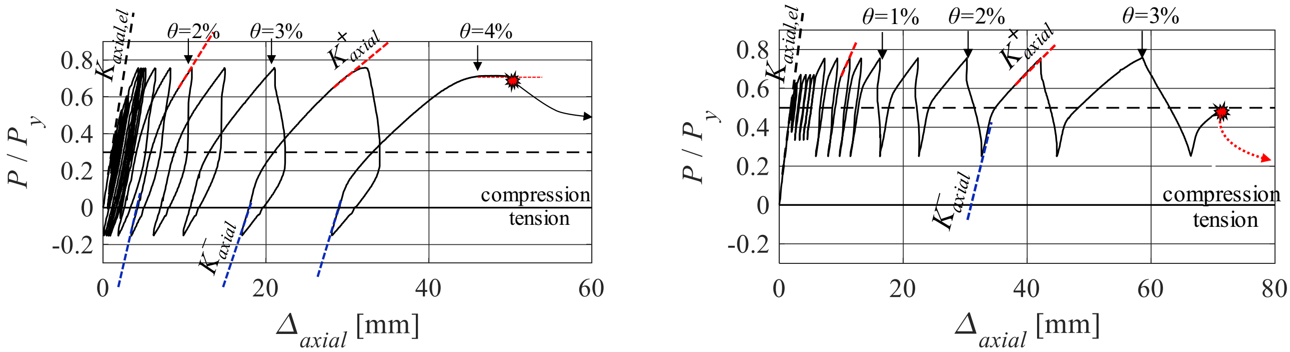

(a) Specimen A4

(b) Specimen B4

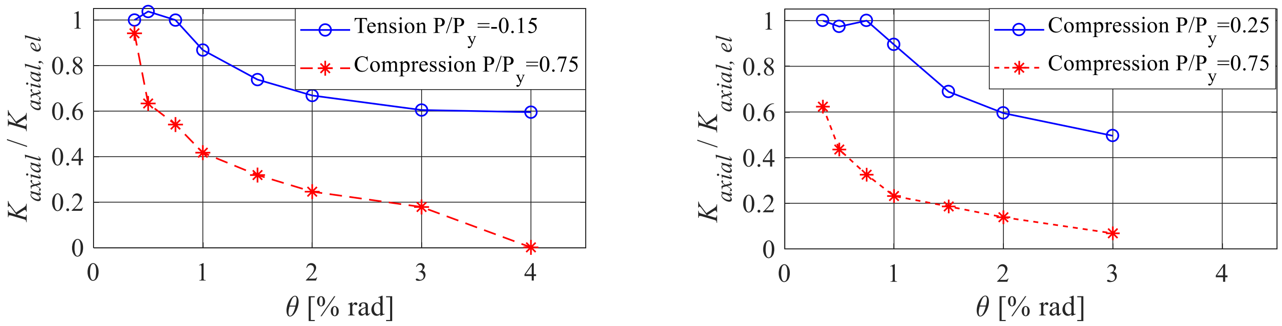

(c) Specimen A4

(d) Specimen B4

Fig. 10. Variable axial load demands and corresponding column axial stiffness deterioration.

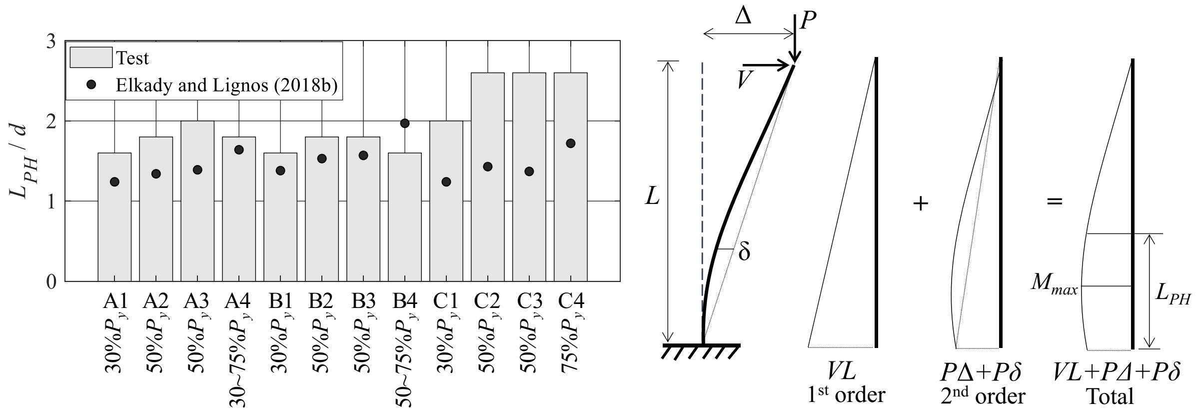

(a) Measured and predicted platic hinge length (b) second-order effects on plastic hinge length

Fig. 11. Assessment of column plastic hinge length.

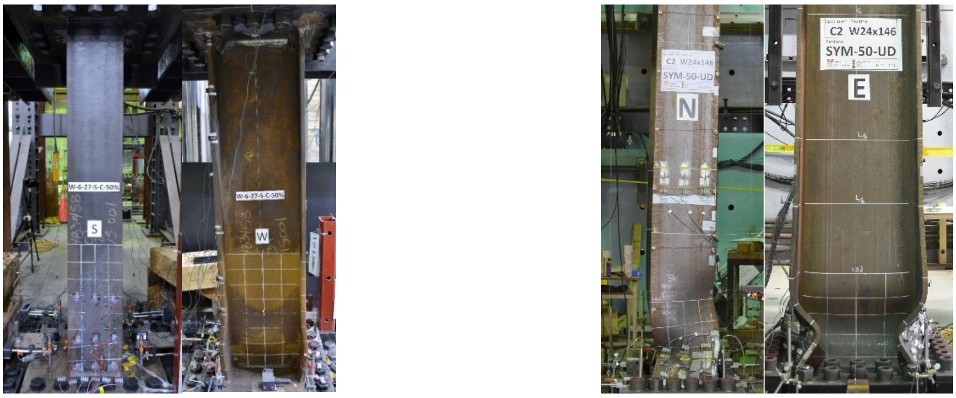

(a) Deformation profile at 2% drift W16x89 (1.8m cantilever)

(b) Deformation profile at 2% drift W24x146 (4m fixed-end)

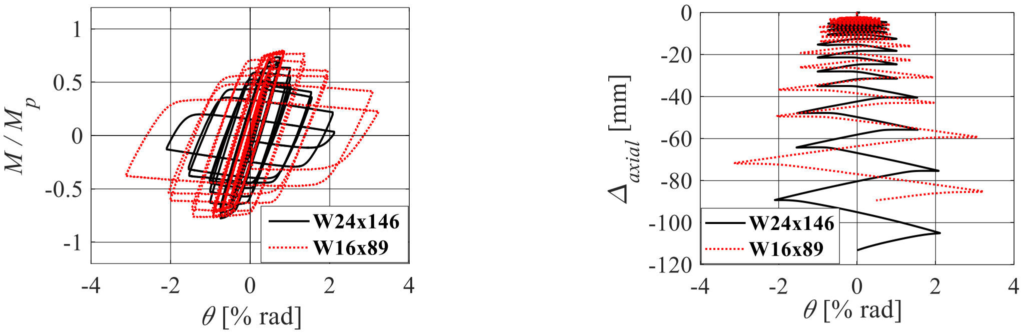

(c) Moment-rotation behavior at column base

(d) Axial shorteing-rotation behavior

Fig. 12. Comparison of column specimens with different cross-section depths and end boundary conditions.

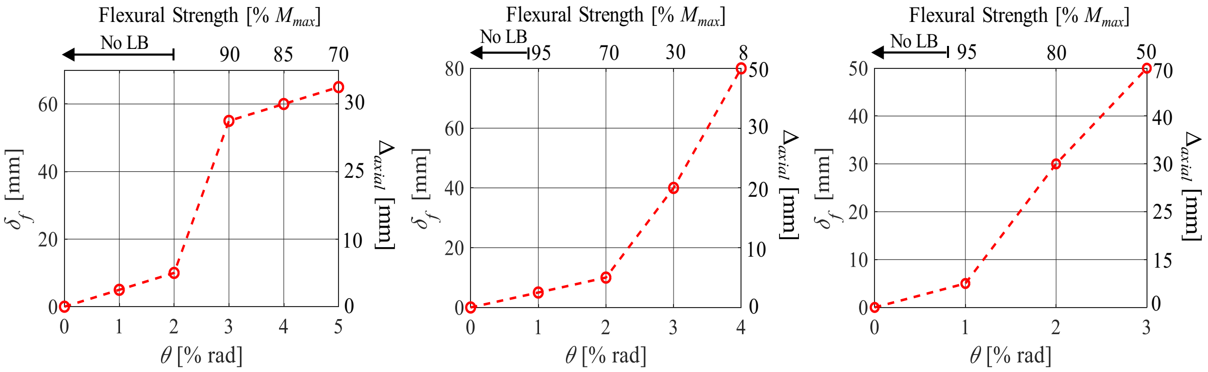

(a) Specimen A3
(Collapse consistent - P/P_y=50%)

(b) Specimen A4
(Symm. - P_g/P_y=30%±P_v/P_y=45%)

(c) Specimen B3
(Symm. - P/P_y=50%)

Fig. 13. Typical column repairability curves.

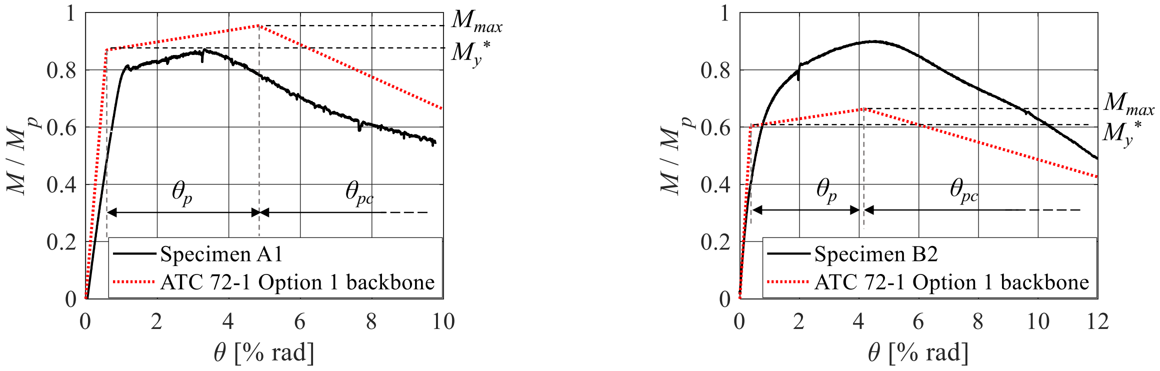

(a) Specimen A1

(b) Specimen B2

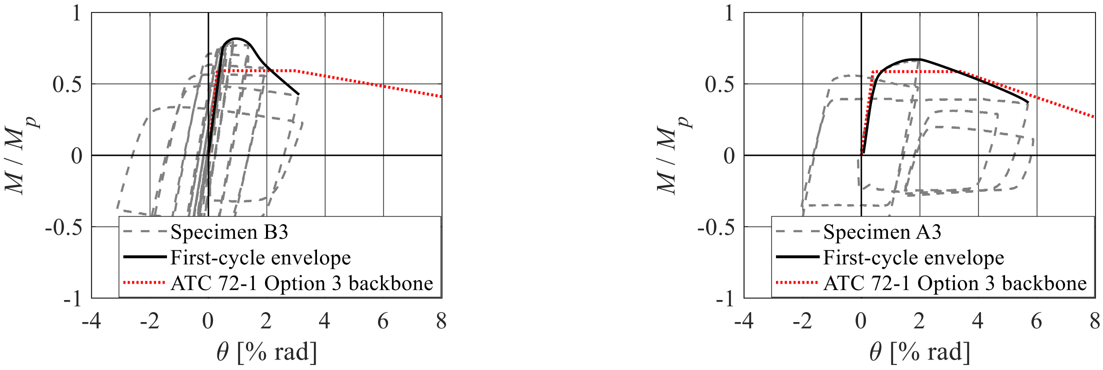

(c) Specimen B3

(d) Specimen A3

Fig. 14. Assessment of PEER/ATC 72-1 modeling guidelines for monotonic and first-cycle envelope curves of wide-flange steel columns.

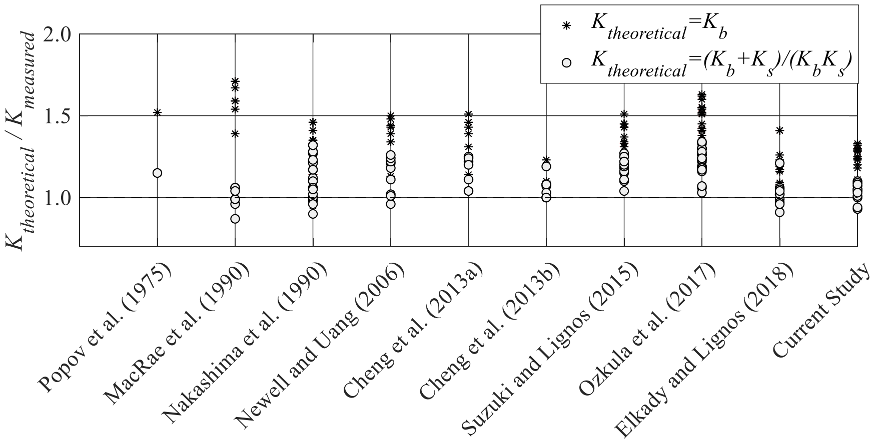

Fig. 15. Ratio of theoretical-to-measured rotational stiffness for several past experimental programs.

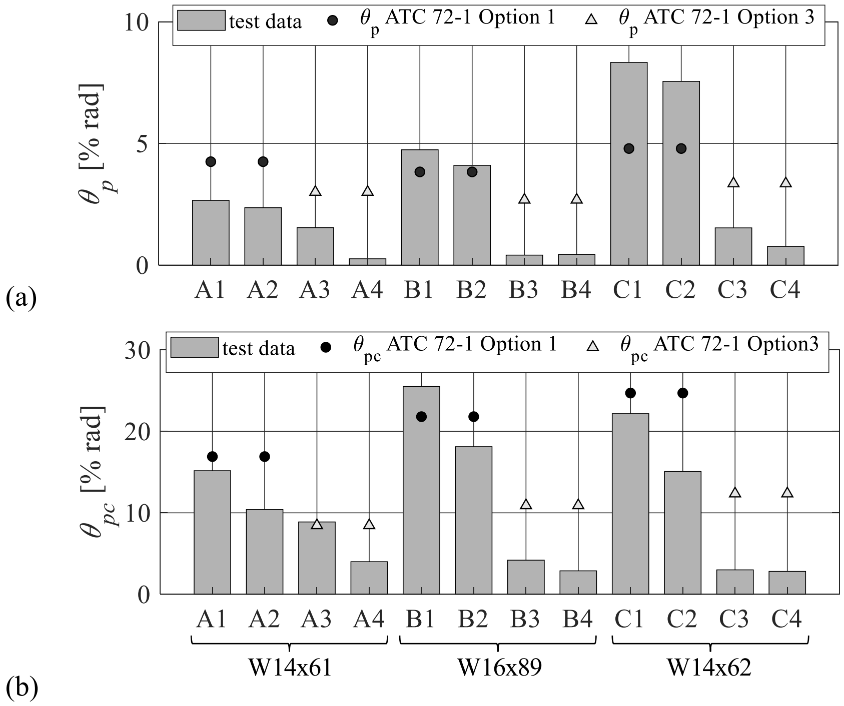

Fig. 16. Assessment of predicted (a) pre- and (b) post-capping plastic rotations of wide-flange steel columns based on PEER/ATC 72-1 modeling recommendations.

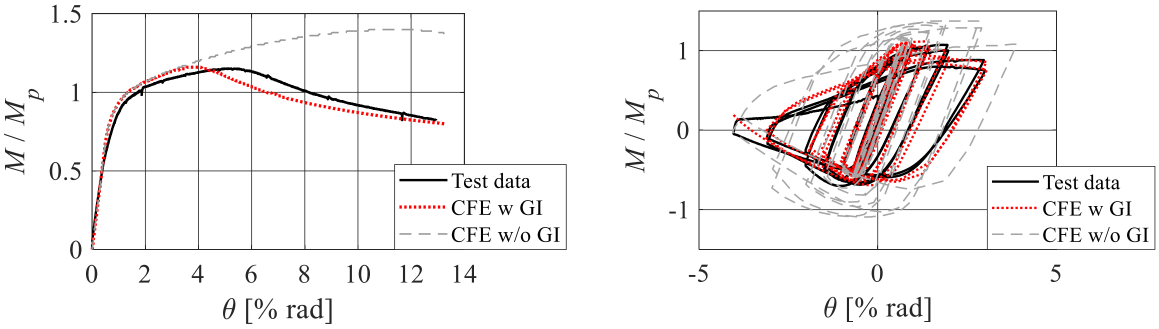

(a) Specimen B1 (W16x89)
(Monotonic – P/P_y =30%)

(b) Specimen A4 (W14x61)
(Symm. – P_g/P_y=30%±P_v/P_y=45%)

Fig. 17. Comparisons between CFE predictions and measured steel column hysteretic response.

List of Figures